University of Iowa

Iowa Research Online

2008

Local lung tissue expansion analysis based on inverse consistent image registration

Kunlin Cao
University of Iowa

Recommended Citation

Cao, Kunlin. "Local lung tissue expansion analysis based on inverse consistent image registration." MS (Master of Science) thesis, University of Iowa, 2008.
https://doi.org/10.17077/etd.yv6lllig

LOCAL LUNG TISSUE EXPANSION ANALYSIS BASED ON INVERSE

CONSISTENT IMAGE REGISTRATION

by

Kunlin Cao

A thesis submitted in partial fulfillment of the
requirements for the Master of Science
degree in Electrical and Computer Engineering
in the Graduate College of
The University of Iowa

May 2008

Thesis Supervisor: Associate Professor Gary E. Christensen

Graduate College
The University of Iowa
Iowa City, Iowa

CERTIFICATE OF APPROVAL

MASTER'S THESIS

This is to certify that the Master's thesis of

Kunlin Cao

has been approved by the Examining Committee for the thesis requirement for the Master of Science degree in Electrical and Computer Engineering at the May 2008 graduation.

Thesis Committee:

Gary E. Christensen, Thesis Supervisor

Joseph M. Reinhardt

Madhavan L. Raghavan

Xiaodong Wu

ACKNOWLEDGEMENTS

I would first of all like to thank Prof. Gary Christensen for his patient support and guidance for this work and the classes he had taught. I would also like to thank Prof. Joseph Reinhardt and Prof. Madhavan Raghavan in BME Department for their great support in this work. I sincerely thank my workmate Kai Ding for his hard work in this project. Great thanks to Joo Hyun Song, Xiujuan Geng and Dinesh Kumar for their help and friendship. Special thanks goes to Dr. Eric Hoffman at Radiology Department for providing data and valuable suggestions for this work. I would also like to thank Prof. Xiaodong Wu and other faculty, staff and students at the IIBI for many informative seminars and lectures.

TABLE OF CONTENTS

LIST OF TABLES

LIST OF FIGURES

CHAPTER 1
INTRODUCTION

1.1 Motivation and Background

The lung is a highly elastic organ. During the respiratory cycle, lung experiences expansion and contraction. Pulmonary diseases, such as fibrosis and emphysema, or injury conditions can cause lung material properties to change and thus its mechanics change. Therefore, understanding and modeling lung mechanics is important to help detect lung diseases or injuries.

Various attempts have been made to study lung function non-invasively. Xenon-enhanced CT (Xe-CT) has been used to measure regional ventilation by observing the Xenon gas wash-in and wash-out rate on serial CT images [18, 25, 2]. But Xenon gas has an anesthetic effect, and Xe-CT imaging is expensive and requires special equipment. In addition, the axial coverage of Xe-CT is limited to a few slices at a time due to its high temporal resolution requirement. Some researchers used non-rigid registration to track lung motion, and studied the relationship between regional lung expansion and ventilation. Guerrero et al. used optical-flow registration to calculate dynamic regional ventilation images from 4D CT images [13, 12]. They showed a close correlation between calculated global lung ventilation and directly measured total lung volume change, but they can not make comparison between regional lung ventilation and local lung expansion due to the limitation of their experiment methods. In addition, they did not show the accuracy of the registration results on the

experimented data. Sundaram et al. used non-linear registration of serial magnetic resonance (MR) images to quantify lung kinematics [23, 24], but lung MRI requires special equipment for gas hyperpolaring during imaging process, and it has low spatial resolution. Also, they encountered the challenge of the inability to track the same point in successive images consistently. Christensen et al. [10, 4] used inverse consistent image registration to register consecutive CT image volumes collected from a multislice CT scanner over multiple breathing periods, and estimate the local tissue expansion and contraction during the respiratory cycle. They showed that the measurements resulted from registration correlated well with spirometry data. However, it was not possible to make comparison between the registration-based estimates and regional tissue ventilation using that method. Thus, it is interesting to model the lung expansion and compare the local lung tissue expansion measures with regional ventilation. Also, finding a method to estimate the local lung deformation measures accurately and efficiently at lower cost is useful for practical use.

The goal of this work is to use deformable image registration on multiple respiratory-gated CT images of the lung acquired at different levels of inflation to estimate the local measures of lung tissue expansion. Comparisons between the regional lung expansion estimates and Xe-CT derived measures of regional ventilation were made to validate the measures derived from registration, and to find the suitable pressure change to quantify the lung expansion characteristics.

1.2   Outline

Chapter 2 discusses the data, data acquisition, and methods used in this work. This chapter also describes the image registration, the inverse consistent image registration algorithm, and the procedure for applying the registration algorithm on the data sets. The methods used for assessing image registration accuracy, calculating local lung tissue expansion and strain measures are described next. The chapter concludes with a brief description of the Xenon CT specific ventilation analysis, and the method used to compare the measures estimated from registration to Xe-CT derived regional ventilation measure.

Chapter 3 presents the registration results. This chapter discusses the registration accuracy, presents the local tissue expansion and strain estimates resulted from registration, compares registration derived measures with regional ventilation from Xe-CT analysis, and shows experiment results using mutual information registration.

Chapter 4 discusses some problems encountered and explores future extensions. And Chapter 5 summarizes this thesis work.

CHAPTER 2
METHODS

2.1   Data Acquisition

Six adult sheep were used for this work. The image data were acquired using a Siemens Sensation 64 multi-detector CT scanner (MDCT) (Siemens Medical Solutions; Erlangen, Germany) with the sheep in the supine position. The animals were anesthetized and mechanically ventilated during the experiments.

2.1.1   Respiratory-Gated CT Data Acquisition

Volumetric CT scans covering the thorax were acquired at six different levels of positive end expiratory pressure (PEEP): 0, 5, 10, 15, 20, and 25 cm H_2O (pitch 1, slice collimation 0.6 mm, rotation time 0.5 sec, slice thickness 0.75 mm, slice separation 0.5 mm, 120kVp, 100 mAs, Kernel B30f). They are denoted as the $P0$, $P5$, $P10$, $P15$, $P20$, and $P25$ images. The data sets are in rigid alignment after acquisition since the sheep were anesthetized and all of the images were acquired without moving the sheep between scans [20].

All CT data were stored in 16-bit Analyze^{TM} (Mayo Clinic, Rochester, MN) format. The image dimension of the transverse view is 512×512, and the z-dimension varies from 587 to 729. The first two sheep AS60133 and AS60150 had voxel size of $0.51 \times 0.51 \times 0.5$ mm^3 while the other four sheep AS70077, AS70078, AS70079 and AS70080 had voxel size of $0.55 \times 0.55 \times 0.5$ mm^3.

2.1.2   Xenon CT Data Acquisition

For Xe-CT studies, twelve contiguous axial locations were selected from the the whole lung volumetric scan at the end expiratory point during the respiratory cycle. The images were gathered as the sheep breath six to eight breaths of room air, then followed approximately 40 breaths of pure xenon gas (wash-in phase) [20].

The Xe-CT were acquired at pressure 0 cm H_2O airway pressure ($P0$) for all six sheep and 10 cm H_2O airway pressure ($P10$) for the last four sheep, and they only cover a limited field of interest. The Xe-CT image dimension for the first two sheep is $512 \times 512 \times 6$ with voxel size $0.51 \times 0.51 \times 3$ mm^3. For the remaining four sheep the Xe-CT image dimension is $512 \times 512 \times 12$ with voxel size $0.55 \times 0.55 \times 2.4$ mm^3.

2.2   Image Registration

2.2.1   Introduction to Image Registration

Image registration has many uses in medical fields such as multi-modality fusion, image segmentation, deformable atlas registration, and measuring growth and modeling motion. The fundamental assumption in each of these applications is that image registration can be used to define a meaningful correspondence mapping between anatomical images collected from imaging devices such as CT, MRI, etc.

Given two images called *template T* and *target S*, a registration procedure to register T to S is finding the optimal correspondence mapping or transformation which deforms T to S. There are different criteria for image registration: minimizing the relative overlap difference, maximizing the mutual information between two images, minimizing the distance between corresponding points of interest called *landmarks*,

etc. All the criteria are designed to find the best correspondence mapping to match image T to S.

2.2.2 Inverse Consistent Image Registration

A meaningful map between two anatomical images should be one-to-one, i.e., each point in image T is mapped to only one point in image S and vice versa. However, the forward mapping from T to S and the reverse mapping from S to T resulted from many unidirectional image registration techniques are not inverses of each other. This inconsistency is resulted from the inability to uniquely describe correspondences between two images during the registration process. Figure 2.1 illustrates the mapping ambiguity problem and the inverse consistency error involved in the image registration algorithm.
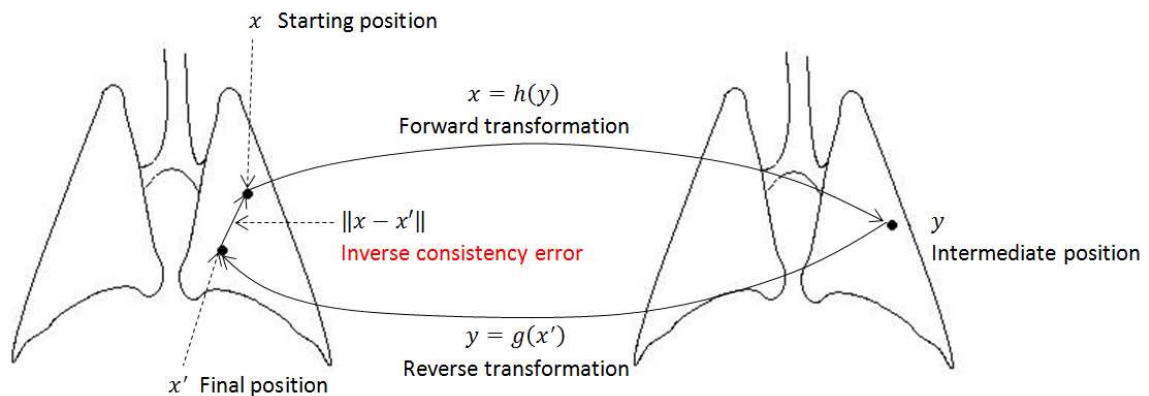
Figure 2.1: An illustration of the mapping ambiguity problem and the inverse consistency error involved in the image registration of two images.

Christensen et al. [6, 5, 7, 16] have introduced a method for image registration

that jointly estimates the forward and reverse transformations between two images while minimizing the inverse consistency error. For a particular registration algorithm, the joint estimation of a consistent set of forward and reverse transformations gives better registration results compared with estimating the two transformations independently.

The image registration algorithm is formulated on the continuum and is discretized for implementation. Suppose T and S represent the template and the target images which are three-dimensional image volumes of voxels dimension $N_1 \times N_2 \times N_3$. Let $\Omega_d = \{(n_1, n_2, n_3) | 0 \leq n_1 < N_1; 0 \leq n_2 < N_2; 0 \leq n_3 < N_3;$ and $n_1, n_2, n_3 \in \mathbb{Z}\}$ be the discrete voxel lattice coordinates and let $\Omega = [0, 1)^3$ be the corresponding continuous domain. The continuous domain and the discrete domain are related in the normal sampling sense $\Omega_d[n] = \Omega(n/N)$, where n/N is defined as the 3×1 vector $[n_1/N_1, n_2/N_2, n_3/N_3]^T$. The continuous images are generated from discrete images using trilinear interpolation.

Let h and g denote the forward transformation and reverse transformations that map the image coordinate Ω to itself. Assume that $h(x) = x + u(x)$, $h^{-1}(x) = x + \tilde{u}(x)$, $g(x) = x + w(x)$ and $g^{-1}(x) = x + \tilde{w}(x)$ where $h(h^{-1}(x)) = x$ and $g(g^{-1}(x)) = x$. Here $u, w, \tilde{u},$ and $\tilde{w}$ are called displacement fields since they define the transformation in terms of a displacement from a location x. All the transformations and displacements are 3×1 vector-valued functions defined on the Ω.

There are many metrics defining the distance between two images. Minimizing the mean squared intensity difference (MSQ) is an easy and effect way to drive the

registration. The transformations h and g are jointly estimated by minimizing the cost function

$$C = \sigma \int_\Omega |T(h(x)) - S(x)|^2 + |S(g(x)) - T(x)|^2 dx$$
$$+ \chi \int_\Omega ||h(x) - g^{-1}(x)||^2 + ||g(x) - h^{-1}(x)||^2 dx \qquad (2.1)$$
$$+ \rho \int_\Omega ||Lu(x)||^2 dx + \int_\Omega ||Lw(x)||^2 dx$$

where the constants σ, χ and ρ are used to balance the constraints. The first integral of the cost function defines the squared intensity error (shape differences) between the deformed image $T \circ h$ and image S, and the differences between the deformed image $S \circ g$ and image T. The second integral couples the estimation of h and g together and penalizes transformations that are not inverses of each other, i.e., minimizing the inverse consistency error shown in Figure 2.1. The third integral is a linear elastic constraint [9, 8] to ensure that the transformations maintain the topology of the images T and S. This term is used to regularize the forward and reverse displacement fields so that they are smooth and continuous by penalizing large derivatives of the displacement fields. The linear elasticity operator L has the form $Lu(x) = -\alpha \nabla^2 u(x) - \beta \nabla(\nabla \cdot u(x)) + \gamma u(x)$ where $\nabla = \left[\frac{\partial}{\partial x_1}, \frac{\partial}{\partial x_2}, \frac{\partial}{\partial x_3}\right]$ and $\nabla^2 = \nabla \cdot \nabla = \left[\frac{\partial^2}{\partial x_1^2} + \frac{\partial^2}{\partial x_2^2} + \frac{\partial^2}{\partial x_3^2}\right]$ in 3D.

A 3D Fourier series representation [1] is used to parameterize the forward and reverse transformations. Christensen and Johnson [6, 15] describe the Fourier series parameterization used in the consistent registration algorithm in detail. Let $k = [k_1, k_2, k_3]$ and $n = [n_1, n_2, n_3]$. The discretized displacement fields are defined as

$$u_d[n] = \sum_{k \in \Omega_d} \mu[k] e^{j<n,\ \theta[k]>} \tag{2.2}$$

and

$$w_d[n] = \sum_{k \in \Omega_d} \eta[k] e^{j<n,\ \theta[k]>} \tag{2.3}$$

for $n \in \Omega_d$. The basis coefficients are defined as

$$\mu[k] = \frac{1}{N_1 N_2 N_3} \sum_{n \in \Omega_d} u_d[n] e^{-j<n,\ \theta[k]>} \tag{2.4}$$

and

$$\eta[k] = \frac{1}{N_1 N_2 N_3} \sum_{n \in \Omega_d} w_d[n] e^{-j<n,\ \theta[k]>} \tag{2.5}$$

for $k \in \Omega_d$. The reason to use the Fourier series parameterization is that it can simplify the linear elasticity constraint given in Equation 2.1 effectively. Substituting Equations 2.2 and 2.3 into the linear elastic constraint in Equation 2.1, and discretizing the continuous partial derivatives of of L, we get a much simpler form of the regularization term in Fourier field

$$C_{\text{REG}} = \sum_{k \in \Omega_d} \mu^\dagger[k] D^2[k] \mu[k] + \eta^\dagger[k] D^2[k] \eta[k] \tag{2.6}$$

where $\dagger$ is the complex conjugate transpose. $D[k]$ is a real-valued, 3×3 symmetric matrix with elements

$$[D[k]]_{rs} = \begin{cases} 2\alpha(N_1^2(1 - cos(\theta_1[k])) \\ \quad + N_2^2(1 - cos(\theta_2[k])) \\ \quad + N_3^2(1 - cos(\theta_3[k]))) \qquad r = s, \\ \quad + 2\beta N_r^2(1 - cos(\theta_r[k])) + \gamma \\ \beta N_r N_s sin(\theta_r[k]) sin(\theta_s[k]) \qquad r \neq s. \end{cases} \qquad (2.7)$$

In order to implement this algorithm, the cost function given in Equation 2.1 can be discretized as

$$\begin{aligned} C(\mu, \eta) = &\sigma \frac{1}{N_1 N_2 N_3} \sum_{n \in \Omega_d} |T_d[Nh_d[n]] - S_d[n]|^2 + |S_d[Ng_d[n]] - T_d[n]|^2 \\ &+ \chi \frac{1}{N_1 N_2 N_3} \sum_{n \in \Omega_d} ||u_d[n, r] - \tilde{w}_d[n, r]||^2 + ||w_d[n, r] - \tilde{u}_d[n, r]||^2 \qquad (2.8) \\ &+ \rho \sum_{k \in \Omega_d[r]} \mu^\dagger[k] D^2[k] \mu[k] + \eta^\dagger[k] D^2[k] \eta[k] \end{aligned}$$

Since the Fourier-series parameterization of the transformation is used in this registration algorithm implementation, there exists a fundamental problem of cyclic boundary conditions. However, when registering full lung volumes, this is not an issue because there is enough information to reduce the effects of edge artifacts.

In this project, the CT images were acquired at different pressures. At higher pressures, more air moves in the lung, thus the intensity range in the lung region is changing between different images. Therefore, intensity difference between the deformed image and target image always exists even in a perfect registration case. The registration problem under this circumstance is similar to the multi-modality

image registration, where mutual information (MI) is widely used as the similarity measure.

Viola and Wells [26, 14] and Collignon and Maes [11, 17, 19] have shown that mutual information works effectively especially in registering images from different modalities. When applied in image registration field, mutual information expresses the amount of information that one image A contains about the other one B

$$I(A, B) = H(A) + H(B) - H(A, B) \tag{2.9}$$

where $H(A)$, $H(B)$ denote the marginal entropies of A and B respectively, while $H(A, B)$ denotes the joint entropy between A and B. The mutual information is maximized when the images are aligned.

Maes [19] introduced the method to measure mutual information between two images. Let N_T and N_S represent the numbers of uniform bins along the respective dimension of the joint histogram constructed by the template image T_d and S_d, and they are indexed by $i \in [0, N_T)$ and $j \in [0, N_S)$. In order to reduce the quantization effects resulted by discretization and interpolation, the continuous estimates of the image distributions is generated using Parzen window. A cubic B-spline kernel $\beta^{(3)}$ is used on the templated image to ensure smoothness and stable derivative calculations. However, since the target image does not contribute to the metric derivatives, simple box kernel $\beta^{(0)}$ is used on the target image. Then the smoothed joint histogram of

the deformed image $T_d \circ h_d$ and target image S_d is

$$p(i,j) = \alpha \sum_{n \in \Omega_d} \beta^{(3)} \left(i - \frac{T_d[Nh_d[n]] - T_d^0}{\Delta b_T} \right) \times \beta^{(0)} \left(j - \frac{S_d[n] - S_d^0}{\Delta b_S} \right) \qquad (2.10)$$

where α is a normalization factor to ensure that $\sum p(i,j) = 1$. $T_d[Nh_d[n]]$ and $S_d[n]$ represent the interpolated deformed images and the target images. They are normalized by he minimum intensity value, T_d^0 or S_d^0, and the bin size, Δb_T or Δb_S, respectively. This aims to fit the intensity value into specified number of bins, N_T and N_S, in the joint intensity distribution.

The marginal probability for the deformed image and target image can be directly calculated from their joint probability

$$p_{T_d \circ h_d}(i) = \sum_j p(i,j),$$
$$p_{S_d}(j) = \sum_i p(i,j). \qquad (2.11)$$

In this program, maximizing the mutual information is converting to minimizing the negative mutual information

$$-I(T_d, S_d) = -\sum_i \sum_j p(i,j) \log \frac{p(i,j)}{p_{T_d \circ h_d}(i) p_{S_d}(j)}. \qquad (2.12)$$

Finally, the mutual information algorithm can be expressed as minimizing the

cost function

$$C(\mu, \eta) = - \lambda \left[I(T_d \circ h_d, S_d) + I(S_d \circ g_d, T_d) \right]$$

$$+ \chi \frac{1}{N_1 N_2 N_3} \sum_{n \in \Omega_d} ||u_d[n, r] - \tilde{w}_d[n, r]||^2 + ||w_d[n, r] - \tilde{u}_d[n, r]||^2 \quad (2.13)$$

$$+ \rho \sum_{k \in \Omega_d[r]} \mu^\dagger[k] D^2[k] \mu[k] + \eta^\dagger[k] D^2[k] \eta[k]$$

where the constants λ, χ and ρ are used to balance the constraints.

2.2.3   Registration Procedure

Before registration, the CT data was converted from 16-bit data to 8-bit un-signed character data using an intensity window that mapped the range from [-1024, 0] HU to [0, 255]. HU values below -1024 are set to 0 and those above 0 are set to 255. Converting the data type enables the algorithm to consume less memory and require less computation time. A more important reason to perform this grayscale mapping is that it highlights the intensity differences between the lung tissue and the sur-rounding chest wall, and the differences between the lung tissue and the airway walls and blood vessels. Figure 2.2 shows an example coronal slice before and after this intensity transformation. After this grayscale mapping, most intensity information is contained in the lung region, and thus no segmentation is needed before registration.

The CT images were down-sampled along each dimension using trilinear in-terpolation. After down-sampling, the voxel size is $1.02 \times 1.02 \times 1$ mm^3 for the first two sheep and $1.10 \times 1.10 \times 1$ mm^3 for the other four sheep. The voxel size for each sheep data is approximately isotropic. The down-sampling processing aims to

(a) (b)
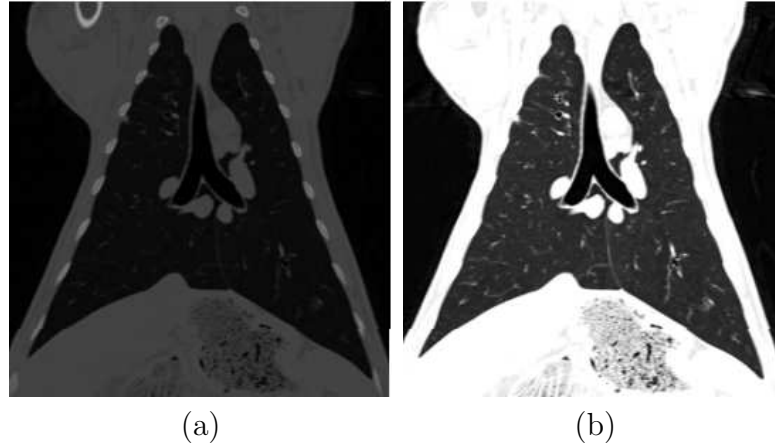
Figure 2.2: The intensity transformation maps the CT values to 8-bit unsigned character data before registration. (a) Original CT data. (b) Data after intensity mapping.

conserve memory required to run the registration software and speed up the process.

No rigid registration is required prior to deformable registration since the animals were not moved between scans and thus were already in rigid alignment, as described in 2.1.1.

After the preprocessing, the volumetric images were registered pairwise according to airway pressure. There are three methods of choosing images to make up the registration pair. In the first method, the pressure change was fixed at 5 cm H_2O. This method generates 5 pairs of registration: $P0$ to $P5$, $P5$ to $P10$, $P10$ to $P15$, $P15$ to $P20$, and $P20$ to $P25$. In the second method, increasing pressure changes from P0 were considered, and another 5 pairs of registration are formed: $P0$ to $P5$, $P0$ to $P10$, $P0$ to $P15$, $P0$ to $P20$, and $P0$ to $P25$. In the third method, increasing pressure changes from P10 were considered. This method produces 3 pairs of registration: $P10$ to $P15$, $P10$ to $P20$, and $P10$ to $P25$.

In the registrations, the weighting constants in the cost function given in Equation 2.8 were set as $\sigma = 1$, $\chi = 600$, and $\rho = 0.00125$. This is the empirical setting for CT-to-CT registration using the inverse consistent image registration algorithm [6]. For mutual information registration, 50×50 histogram bins were used, and the weighting constants in the cost function given in Equation 2.13 were set as $\lambda = 0.1$, $\chi = 600$, and $\rho = 0.00125$.

A spatial and frequency multiresolution procedure was used in the registration in order to improve speed, accuracy and robustness. The basic idea is that registration is first performed at a coarse scale and the transformation estimated at the coarse scale is used to initialize registration at the next finer scale. This process is repeated until it reaches the finest scale. This coarse-to-fine scheme matches the the global structures before local in order to eliminate local optima at coarser scales. The multiresolution strategy used in the experiments proceeds from low to high resolution starting at one-eighth the spatial resolution and increases by a factor of two until the full resolution is reached. The multiresolution schemes for minimizing the cost function given in Equation 2.8 (MSQ registration) and for minimizing the cost function given in Equation 2.13 (MI registration) are shown in Table 2.1.

Note that for most cases, the mean squared intensity difference is used as similarity measure to drive the registration. The results obtained using mutual information as the similarity measure is mentioned and discussed later. If there is no mention about mutual information, the registration is driven by the mean squared intensity difference.

Table 2.1: Multiresolution schemes for MSQ and MI registration

Resolution	MSQ		MI	
	Step size	Iterations	Step size	Iterations
0.125	0.0001	500	0.00001	500
0.25	0.0001	500	0.00001	500
0.5	0.0001	100	0.000001	100
1	0.0001	20	0.000001	50

After completing the registration process, the voxel-by-voxel displacement fields between each image pair were generated and used to track the local lung tissue motion during the respiratory cycle.

2.3 Assessment of Registration Accuracy

2.3.1 Tracking landmarks movement

Anatomic landmarks were manually selected and tracked in all six images for five sheep in order to assess the registration accuracy. The number of landmarks ranged from 9 to 15, and were different for each sheep. These landmarks were chosen as airway branchpoints. Using the displacement fields determined by the image registration for each image pair, the landmarks in the template image were mapped to the target image. Then the estimated landmark position was compared to the actual landmark position in the target image, and the landmark position error was calculated, as shown in Figure 2.3.

2.3.2 Transitivity Error Analysis

As discussed in 2.2.2, a meaningful registration should have zero or nearly zero inverse consistency error. In this project, since there are many registration
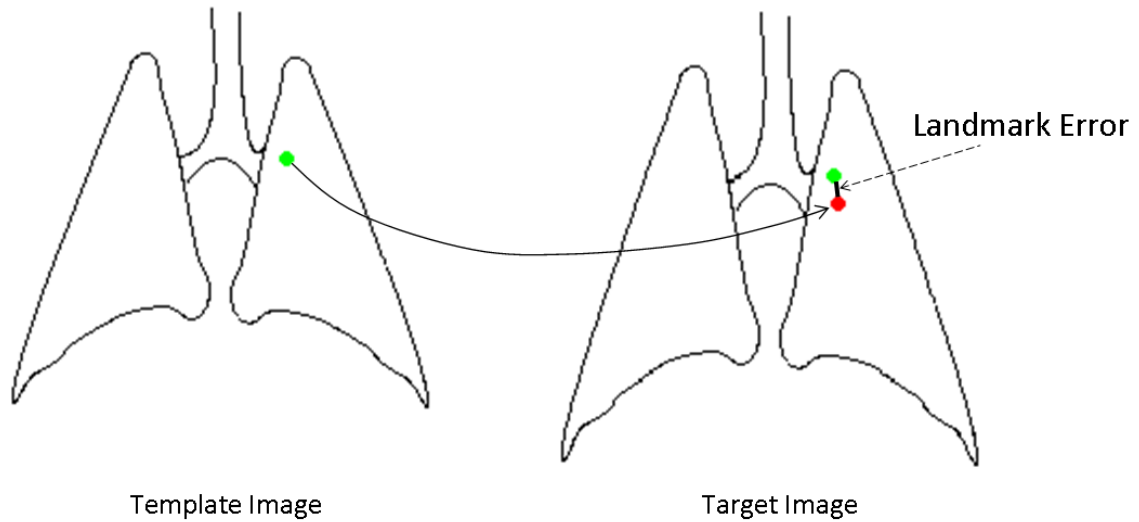
Figure 2.3: Illustration of the landmark error. The green landmark in template image should correspond to the green point in target image. Registration maps the green landmark in template image to the position marked as red in target image. The distance between the predicted position (red point) and the true position (green point) in target image is defined as landmark error.

pairs, analysis of the transitivity error is useful to check the invertibility property and evaluate the consistency of a group of transformations. The transitivity of a set of transformations is defined by measuring the difference between the identity mapping and the composition of those transformations, as described in Christensen and Johnson [7] and the Non-Rigid Image Registration Evaluation Project (NIREP) [3].

The transitivity property is shown in Figure 2.4. Suppose the points x, y, z are the same landmark appears in three different images A, B, C, respectively. Assume that the set of transformations $H = \{h_{AB}, h_{BA}, h_{BC}, h_{CB}, h_{AC}, h_{CA}\}$ satisfy

the invertibility property

$$y = h_{BA}(x), \quad z = h_{CB}(y), \quad x = h_{AC}(z). \tag{2.14}$$

Performing substitution in the three equations, we achieve the result

$$x = h_{AC}(h_{CB}(h_{BA}(x))). \tag{2.15}$$

This relationship is called transitivity property. From above deductions we can get the conclusion that transformations that are inconsistent are even more difficult to satisfy the transitivity relationship.
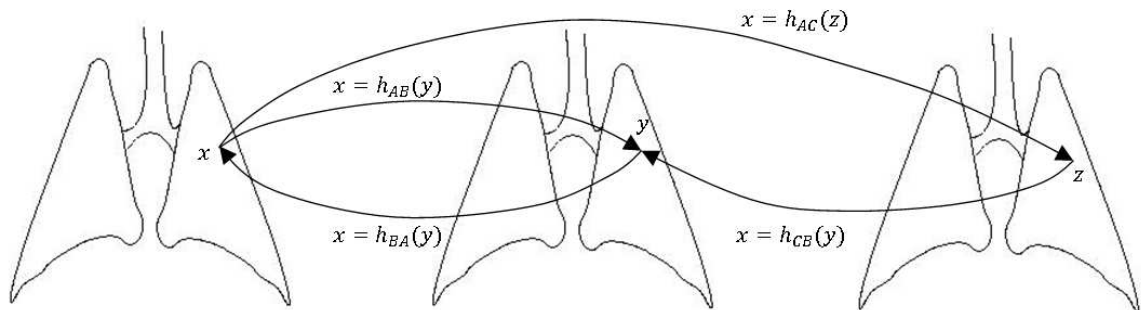

Figure 2.4: Illustration of the transitivity property of a group of transformations.

The average transitivity error of a group of transformations is defined as

$$E_{\mathrm{TC}}(h_{AB}, h_{BC}, h_{CA}, M) = \frac{1}{M} \int_M ||h_{AB}(h_{BC}(h_{CA}(x))) - x||dx \tag{2.16}$$

where M denotes the region of interest (ROI). For a set of transformations, lower average transitivity error indicates more accurate and consistent registrations in general.

In this project two groups of transformations were formed in order to do the transitivity error analysis. The first group couples the transformations from $P0$ to $P5$, $P5$ to $P10$, and $P10$ to $P0$, while the second group couples the transformations from $P10$ to $P15$, $P15$ to $P20$, $P20$ to $P25$, and $P25$ to $P0$. Transitivity error for each group was calculated by estimating the average difference between the identity mapping and the composition of the transformations in the group.

2.4 Estimates of Local Lung Expansion
based on Registration

2.4.1 Specific Volume Change based on Jacobian

The Jacobian is a measurement to estimate the pointwise expansion and contraction during the deformation, and is used to measure the local lung volume change. Assume we have an image I_1 at lower pressure and another image I_2 at higher pressure. Let $h(x,y,z) = [h_x(x,y,z), h_y(x,y,z), h_z(x,y,z)]^T$ be the transformation and $u(x,y,z) = [u_x(x,y,z), u_y(x,y,z), u_z(x,y,z)]^T$ be the corresponding displacement deforms the template image I_1 to the target image I_2. The relationship between $h(x,y,z)$ and $u(x,y,z)$ is shown in 2.2.2: $h(x,y,z) = (x,y,z) + u(x,y,z)$. Then, a voxel at location (x,y,z) in image I_1 is displaced by $u(x,y,z)$ to map to its correspondence in image I_2. The Jacobian $J(x,y,z)$ of the transformation is defined as

$$J(x, y, z) = \begin{vmatrix} \frac{\partial h_x(x,y,z)}{\partial x} & \frac{\partial h_x(x,y,z)}{\partial y} & \frac{\partial h_x(x,y,z)}{\partial z} \\[2ex] \frac{\partial h_y(x,y,z)}{\partial x} & \frac{\partial h_y(x,y,z)}{\partial y} & \frac{\partial h_y(x,y,z)}{\partial z} \\[2ex] \frac{\partial h_z(x,y,z)}{\partial x} & \frac{\partial h_z(x,y,z)}{\partial y} & \frac{\partial h_z(x,y,z)}{\partial z} \end{vmatrix}$$

$$= \begin{vmatrix} 1 + \frac{\partial u_x(x,y,z)}{\partial x} & \frac{\partial u_x(x,y,z)}{\partial y} & \frac{\partial u_x(x,y,z)}{\partial z} \\[2ex] \frac{\partial u_y(x,y,z)}{\partial x} & 1 + \frac{\partial u_y(x,y,z)}{\partial y} & \frac{\partial u_y(x,y,z)}{\partial z} \\[2ex] \frac{\partial u_z(x,y,z)}{\partial x} & \frac{\partial u_z(x,y,z)}{\partial y} & 1 + \frac{\partial u_z(x,y,z)}{\partial z} \end{vmatrix}. \tag{2.17}$$

In this way, the Jacobian at each voxel location can be calculated to estimate the local lung tissue deformation. In a Eulerian reference frame, a Jacobian value of one corresponds to zero expansion or contraction, a value greater than one corresponds to contraction and a value less than one corresponds expansion. A negative Jacobian value is undesired because it implies that the transformation is folded and thus the topology is destroyed when transforming images.

For a voxel at location (x, y, z) in image I_1, the Jacobian $J(x, y, z)$ in Lagrangian reference frame expresses the ratio between two volume states V_1 and V_2 for the volume element in I_1 and I_2

$$J(x, y, z) = \frac{V_2}{V_1} = \frac{V_1 + \triangle V}{V_1}, \tag{2.18}$$

where $\triangle V = V_2 - V_1$ is the local volume change due to inspiration. Specific volume

change is solved by rearranging Equation 2.18 [20]

$$\frac{\triangle V}{V_1} = J(x,y,z) - 1. \tag{2.19}$$

2.4.2 Specific Volume Change based on

CT Intensity Change

The lung density is represented by CT grayscale in Hounsfield Units (HU), which is defined such that the HU of water and air are 0 and -1000, respectively. Since the lung density decreased as it inflates with air, changes in the lung CT density during inflation can also be used to quantify regional mechanical properties. Therefore, given CT images of a lung region at two different pressures, it is possible to calculate its density change and estimate the regional volume change based on registration results.

Simon [22] reported a relationship between registered CT regional values and the regional volume change. After registration, the mapping of each voxel between I_1 and I_2 allows us to identify the corresponding tissue elements. $3\ mm \times 3\ mm \times 3\ mm$ local averaging of the CT HU for both I_1 and I_2 is preformed since the mapping may contain some error [13]. Let HU_1 and HU_2 be the CT grayscale for I_1 and I_2, respectively. Simon's method assumes that the fraction of air in a region is given by

$$F_{air} = -\frac{HU}{1000}. \tag{2.20}$$

Thus, the air fraction for the same region in I_1 and I_2 is

$$F_1 = -\frac{HU_1}{1000}, \quad F_2 = -\frac{HU_2}{1000}. \tag{2.21}$$

According to Simon [22],

$$\frac{\triangle V}{V_1} = \frac{F_2 - F_1}{F_1(1 - F_2)}, \tag{2.22}$$

where V_1 is the original volume and $\triangle V = V_2 - V_1$ is the local volume change due to inspiration. Specific volume change is expressed by CT grayscale after substituting Equation 2.21 to Equation 2.22

$$\frac{\triangle V}{V_1} = 1000\frac{HU_2 - HU_1}{HU_1(1 + HU_2)}. \tag{2.23}$$

In our study, we segmented out the lung region using Analyze$^{\text{TM}}$ software, and applied Equation 2.23 on all the local lung tissue that contain between 40% and 90% air to generate the ventilation parametric image representing local specific volume change. Then a $9\ mm \times 9\ mm \times 9\ mm$ spatial averaging of the ventilation parametric images was performed in order to generate the final 3D ventilation map [13].

2.5   Strain Analysis

From the displacement fields estimated in registration process, strain can be calculated to express the geometrical deformation caused by the action of stress in the lung.

The linear strain along x, y, and z axes are defined as the fractional length

change

$$\epsilon_x = \frac{\partial u_x}{\partial x}, \quad \epsilon_y = \frac{\partial u_y}{\partial y}, \quad \epsilon_z = \frac{\partial u_z}{\partial z} \tag{2.24}$$

where $u = [u_x, u_y, u_z]^T$ is the 3D displacement field. Similarly the angular change at any point between two lines crossing this point before and after deformation can be measured as a shear strain. The shear strain are defined as

$$\begin{aligned}
\epsilon_{xy} &= (\frac{\partial u_x}{\partial y} + \frac{\partial u_y}{\partial x})/2 = \epsilon_{yx}, \\
\epsilon_{yz} &= (\frac{\partial u_y}{\partial z} + \frac{\partial u_z}{\partial y})/2 = \epsilon_{zy}, \\
\epsilon_{xz} &= (\frac{\partial u_x}{\partial z} + \frac{\partial u_z}{\partial x})/2 = \epsilon_{zx}.
\end{aligned} \tag{2.25}$$

Linear strain: $\varepsilon_{\mathbf{x}} = \frac{\partial x' - \partial x}{\partial x} = \frac{\partial u_x}{\partial x}$

(a)

Shear strain: $\varepsilon_{\mathbf{xy}} = (\frac{\partial u_x}{\partial y} + \frac{\partial u_y}{\partial x})/2 = \varepsilon_{\mathbf{yx}}$
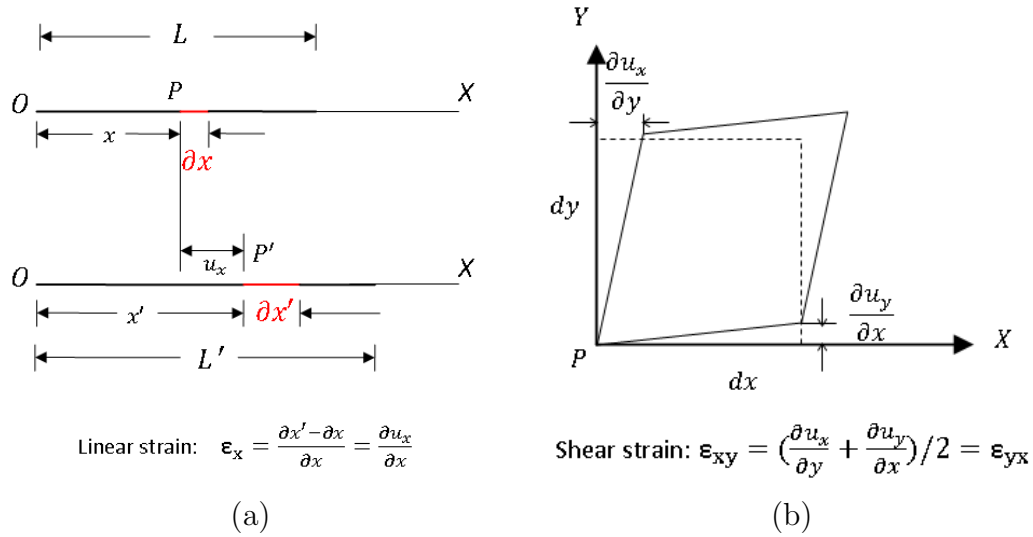
(b)

Figure 2.5: Illustration of (a) 1D linear strain and (b) 2D shear strain.

Figure 2.5 gives an illustration of 1D linear strain and 2D sheer strain. Using

the above notation for linear strain and sheer strain, it is possible to express strain as a symmetric strain tensor

$$\epsilon = \begin{bmatrix} \epsilon_x & \epsilon_{xy} & \epsilon_{xz} \\ \epsilon_{yx} & \epsilon_y & \epsilon_{yz} \\ \epsilon_{zx} & \epsilon_{zy} & \epsilon_z \end{bmatrix} = \frac{1}{2}\left[\nabla u + (\nabla u)^T\right] \tag{2.26}$$

where ∇u is the gradient of the displacement field

$$\nabla u = \begin{bmatrix} \frac{\partial u_x}{\partial x} & \frac{\partial u_x}{\partial y} & \frac{\partial u_x}{\partial z} \\ \frac{\partial u_y}{\partial x} & \frac{\partial u_y}{\partial y} & \frac{\partial u_y}{\partial z} \\ \frac{\partial u_z}{\partial x} & \frac{\partial u_z}{\partial y} & \frac{\partial u_z}{\partial z} \end{bmatrix}. \tag{2.27}$$

The strain tensor is a real symmetric matrix. Then by singular value decomposition (SVD), the strain tensor can be represented as a set of orthogonal eigenvectors, along which there is no shear, but only stretch or compression. The eigenvalues are defined as principal strains, and the eigenvectors are called principal directions.

The ratio of the length in the direction of maximal extension over the length in the direction of minimal extension is defined as anisotropic deformation index (ADI). The ADI value is always larger or equal to 1. A big ADI value indicates an anisotropic expansion, while a ADI values approximately 1 represents an isotropic expansion.

In this thesis work, the strain was calculated from $P0$ to $P10$ in sheep AS70078, and compared with the corresponding Jacobian map in order to get more information about the lung tissue expansion.

2.6 Xenon CT Specific Ventilation Analysis

During the Xenon gas wash-in phase of image acquisition, the Xe-CT time series data shows an exponential rise in lung density. In each ROI to be analyzed, the mean density $D(t)$ is modeled as in [21]

$$D(t) = \begin{cases} D_0 & 0 \leq t < t_0 \\ D_0 + (D_f - D_0)(1 - e^{-\frac{t-t_0}{\tau}}) & t \geq t_0, \end{cases} \quad (2.28)$$

where D_0 is the density in the ROI before switching to xenon gas, D_f is the density when xenon was inspired until equilibrium, t_0 is the start time switching to xenon from room air, and τ is the model time constant. Specific ventilation (sV, ventilation per unit lung air volume in $\min^{-1}$) for each ROI was calculated as the inverse of the time constant τ, i.e., $sV = \tau^{-1}$. A bigger sV value in a ROI indicates larger density change in a time unit.

2.7 Comparison between Estimates
from Registration and sV

2.7.1 Comparison between Jacobian and sV

As air moves in the lung during inflation phase, it results in the lung tissue expansion and density change. The specific ventilation (sV) calculated from Xe-CT estimates the density change, and the Jacobian calculated from registration results measures the local tissue deformation. The lung tissue which has large density change should also have large deformation. Therefore, it is reasonable to expect a direct relationship between these two measures.

Figure 2.6 shows the comparison experiment scheme. There are two groups of experiments. The first group of experiments used 5 sheep data. We compared sV from Xe-CT at $P0$ with the measures from registration $P0$ to $P5$, $P5$ to $P10$, $P10$ to $P15$, $P15$ to $P20$, and $P20$ to $P25$, shown in Figure 2.6(a). The second group of experiments used 4 sheep data. We compared sV from Xe-CT at $P10$ with the measures from registration $P10$ to $P15$, $P15$ to $P20$, and $P20$ to $P25$, shown in Figure 2.6(b).
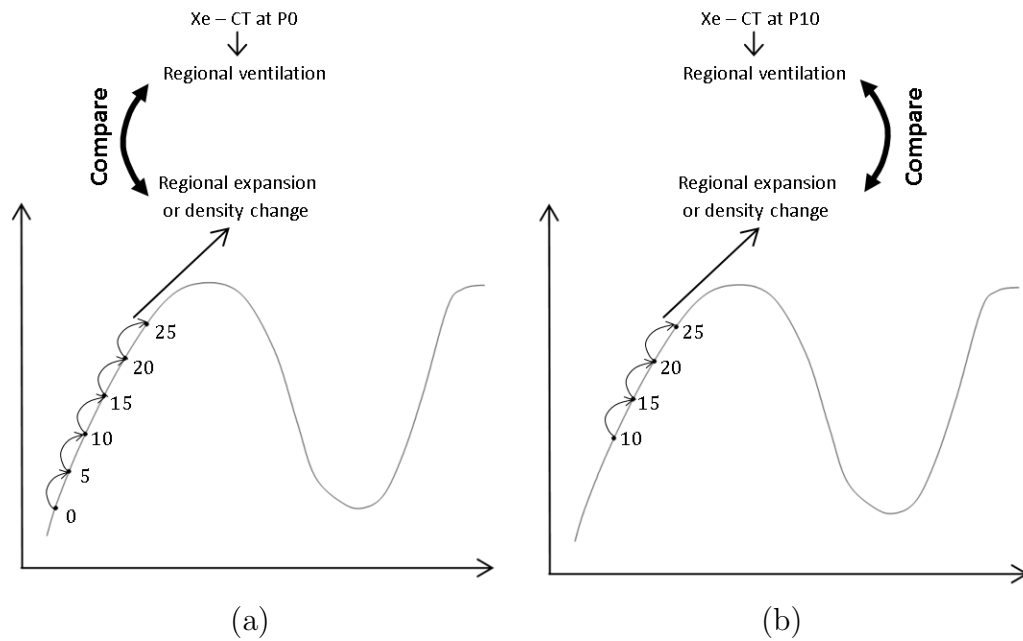

Figure 2.6: Illustration of the comparison experiment scheme from (a) $P0$ and (b) $P10$.

The CT images cover the whole lung region, however, the Xe-CT images only cover limited range along z-dimension. In order to compare the Jacobian from registration results of CT images and the sV from Xe-CT analysis, a rigid registration

is needed to register the Xe-CT slices to a 3D rectangular region in the the starting CT image. In the rectangular region, a filtering process was performed and only the regions that contain between 40% and 90% air were left over for later calculation.
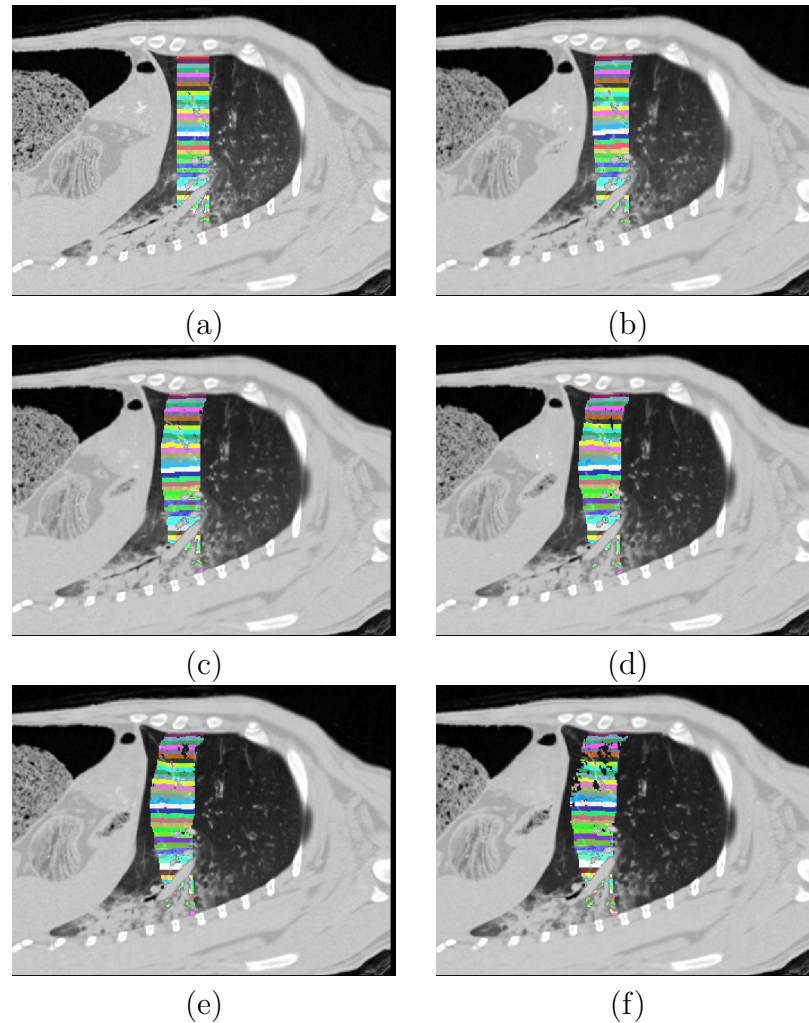

Figure 2.7: Method of Jacobian analysis in the comparison experiment. (a) $P0$ image shows the initial rectangular regions of interest. Subsequent images show how each region deforms as the lung expands. (b) $P5$ image; (c) $P10$ image; (d) $P15$ image; (e) $P20$ image; (f) $P25$ image. These pictures are generated from sheep AS70080.

Within the 3D rectangular region, 30 to 39 slabs were defined which spaced

along y (ventral to dorsal) direction equally. Each slab is 4 mm thick. This spatial encoding is shown in Figure 2.7(a). In order to compare the measurement from CT image registration with sV from Xe-CT acquired at $P0$, the starting CT image to perform spatial encoding was chosen at $P0$. The deformation of each slab can be tracked across the $P5$, $P10$, $P15$, $P20$, and $P25$ images using the displacement fields resulted from registration. This process is shown in Figure 2.7(b)-(f).

Using Xe-CT images at $P10$, the second set of comparison experiments were made in the similar way. The region extraction and spatial encoding process is the same as described above. Instead of defining slabs on $P0$ CT image, the spatial encoding was performed on $P10$ CT image. And the coverage of each slab can be tracked across $P15$, $P20$, and $P25$.

Within each slab, the average measures of Jacobian and sV were calculated and plotted. Then the comparison between Jacobian and sV was made by fitting a linear regression line to the scatter plot. The correlation coefficients r from the linear regression of average Jacobian and average sV was calculated and used to measure how close one estimate is related to the other one [20].

2.7.2   Comparison between Intensity-based

Regional Volume Change and sV

The lung region which has increased volume during respiratory cycle should have decreased mean graylevel due to increased air content. In each slab defined in 2.7.1, the average CT HU was calculated across different pressures. Applying equation 2.23 on each slab, the regional volume change was measured and compared with the

average sV. The correlation coefficients between the two estimates were calculated by linear regression as described above.

CHAPTER 3
RESULTS

3.1   Visualization of Image Registration Results

Registration of one image pair using the Small Deformation Inverse Consistent Linear Elastic (SICLE) algorithm [6, 16] took an average of 40 to 50 minutes on a workstation with dual Intel Xeon 2.33GHz processors and 16 GB of RAM.

An example of registration results is shown in Figure 3.1. Figure 3.1(a) and (b) show coronal slices at $P0$ and $P10$ pressure for sheep AS70080 respectively. The deformed slice from $P0$ image to $P10$ image is shown in Figure 3.1(c). Figure 3.1(d) and (e) show the absolute intensity difference between the template slice and the target slice before registration, and the difference between the deformed template slice and the corresponding target slice after registration. The bright region around the base of lung found in the difference image before registration are significantly reduced after registration, which indicates a successful registration. However, since the air content are different in $P0$ and $P10$ images, the resulted deformed image from $P0$ has different intensity scale with $P10$ image, as shown in Figure 3.1(b) and (c). As a result, the difference between deformed image and target image can never be zero.

The displacement fields estimated in registration process were used in later analysis. Figure 3.2 shows a 2D displacement field for sheep AS70078 from $P0$ to $P10$ on a coronal slice.
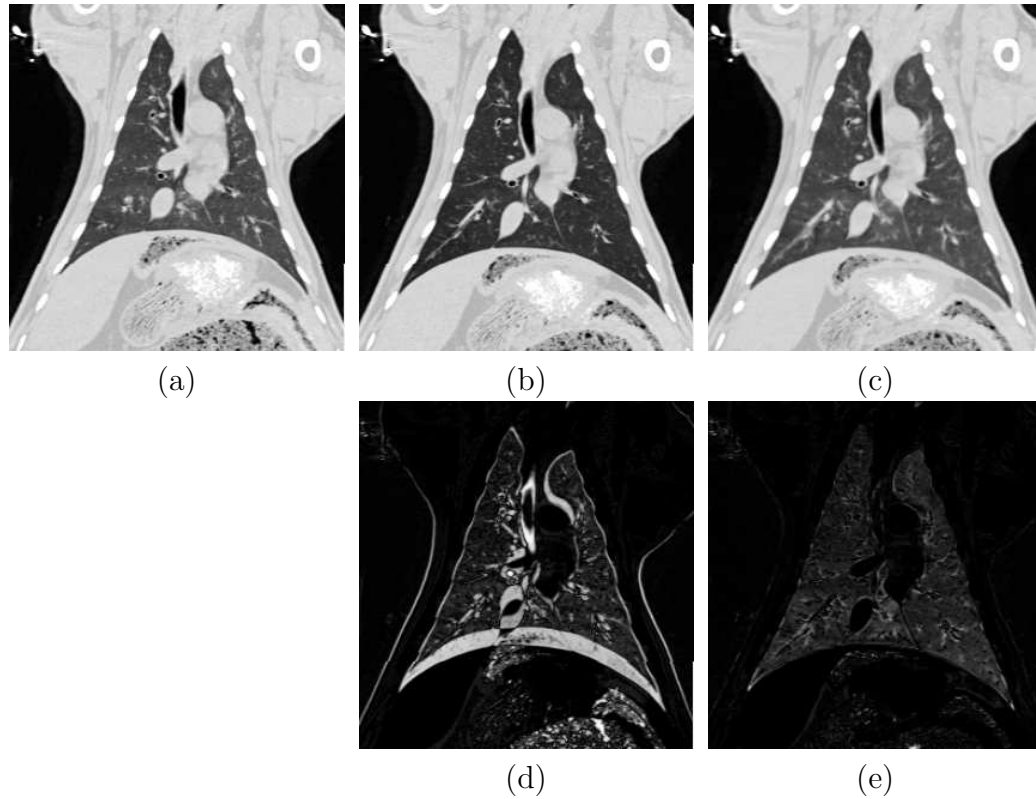
Figure 3.1: Registration example of AS70080. (a) A slice of $P0$ image; (b) a slice of $P10$ image; (c) a slice of deformed image from $P0$ to $P10$ which matches (b); (d) difference between (a) and (b); and (e) difference between (c) and (b).
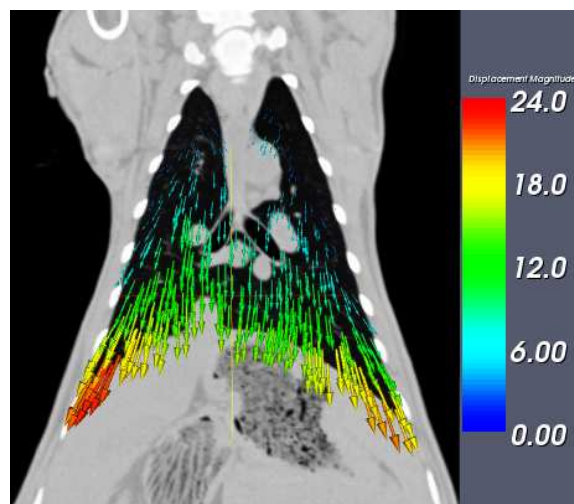

Figure 3.2: 2D displacement field from $P0$ to $P10$ for sheep AS70078 shown on a coronal slice. The red vectors represent larger displacement.

3.2   Assessment of Image Registration Accuracy

3.2.1   Landmark Error

The landmarks were chosen as recognizable airway branchpoints located in the central region of lung, as shown in Figure 3.3 and Figure 3.4.

The registration accuracy measured by predicting landmarks motion across five 5 cm H_2O pressure change pairs $P0$-$P5$, $P5$-$P10$, $P10$-$P15$, $P15$-$P20$, and $P20$-$P25$ for five sheep is shown in Figure 3.5(a). Figure 3.5(b) shows their mean landmark error averaged on five sheep. These data are shown in Table A.1.

Figure 3.5 shows that the average landmark errors for 5 cm H_2O pressure change pairs are small (within 1.5 mm) except one outlier sheep AS60150. This sheep shows large landmark error when transforming images from $P0$ to $P5$. By further inspection of this sheep, atelectasis in the most dorsal lung region was noticed in $P0$ image, shown as the ROI in red rectangle in Figure 3.6(a). However, this fluid region appears normal in the images at $P5$ and higher pressure images, shown in Figure 3.6(b).

The registration is based on intensity matching, thus the lower contrast caused by atelectasis resulted in the larger landmark errors from $P0$ to $P5$. However, starting from $P5$ image, since more air goes into the airway, the intensity contrast is increasing and thus results in more accurate registration. This is a general phenomenon shown in Figure 3.5(b). As the contrast increased at higher pressure images, the registrations are tend to be more accurate and results in smaller landmark errors.

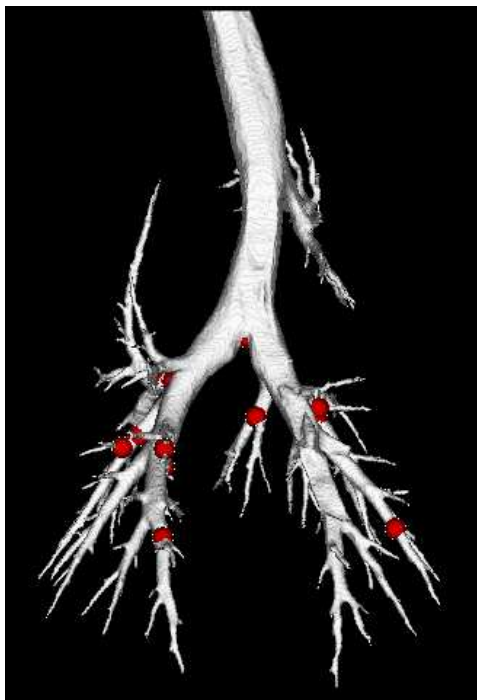The registration accuracy measured by predicting landmarks motion across in-

Figure 3.3: Landmark positions on the airway tree segmented out from sheep AS60133 at 0 cm H_2O airway pressure.
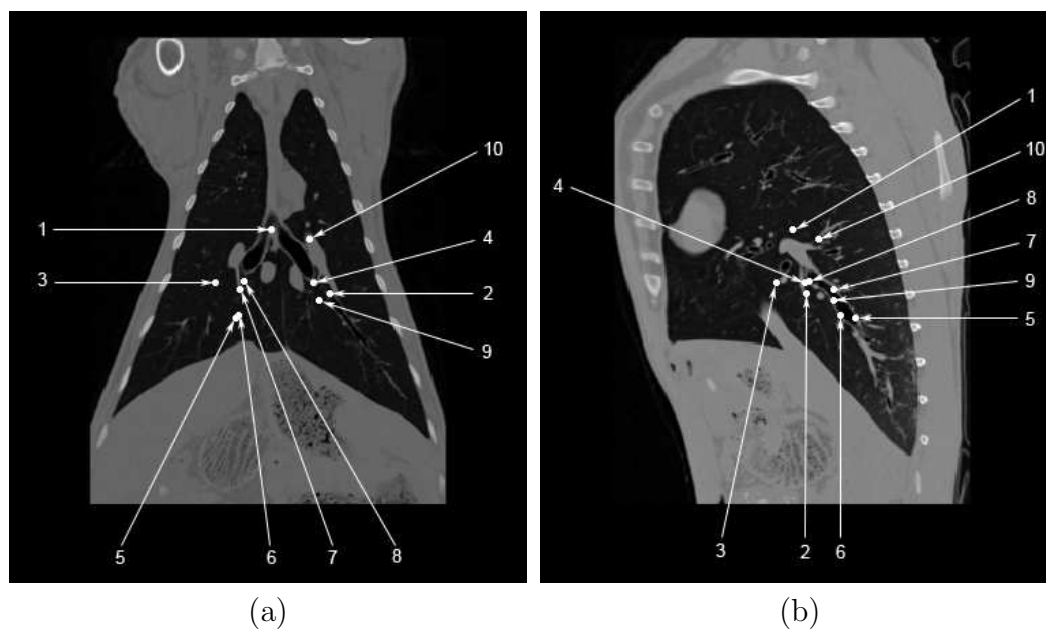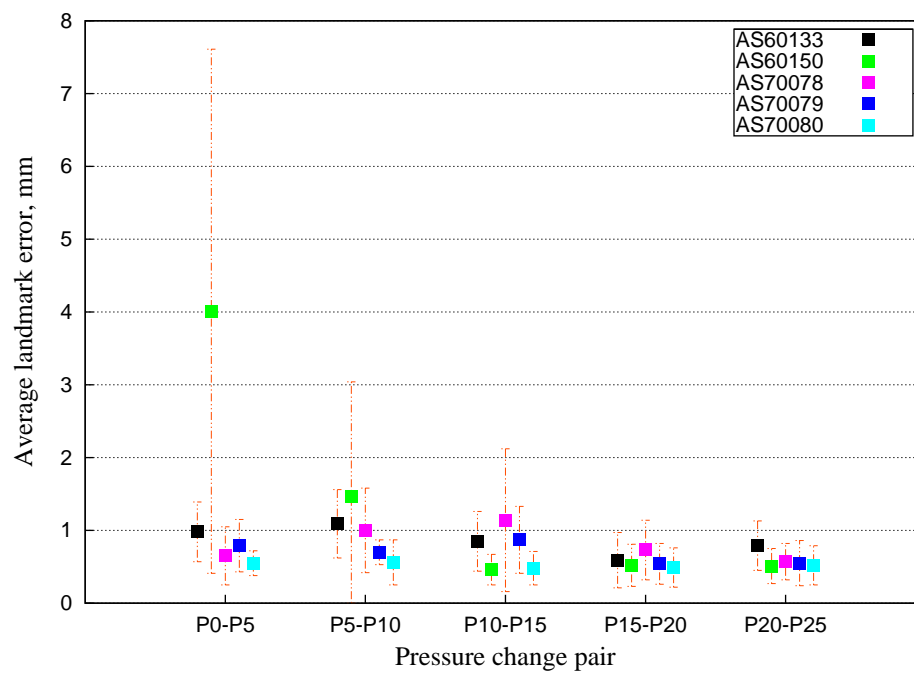

(a)   (b)

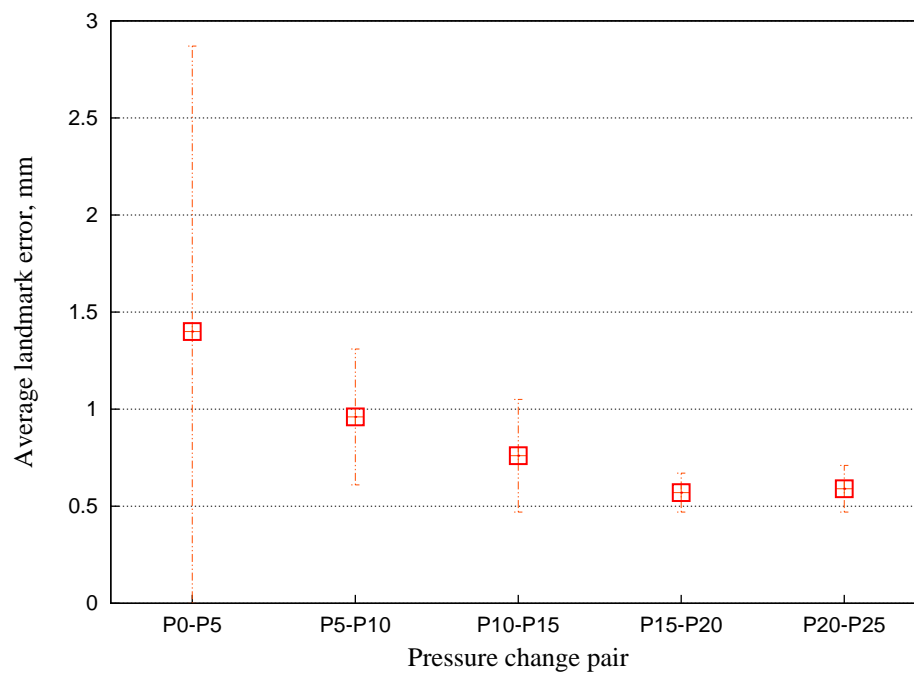Figure 3.4: Projection of landmark positions onto (a) a coronal slice and (b) a sagittal slice for sheep AS70078 at 25 cm H_2O airway pressure.

Figure 3.5: Registration accuracy for the 5 cm H_2O pressure change pairs. (a) Mean landmark errors for each animal for each pressure change pair. (b) Mean landmark errors for each pressure change pair averaged across all five sheep.
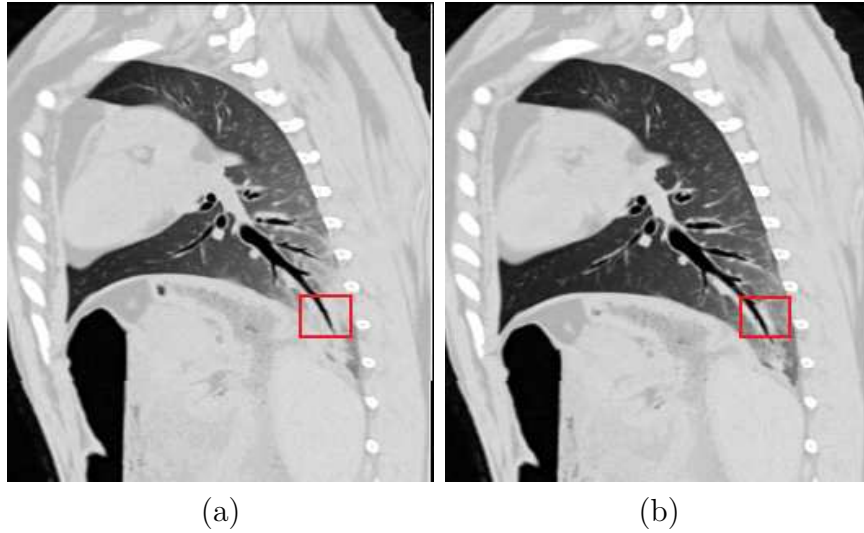
Figure 3.6: Atelectasis in sheep AS60150. (a) The atelectasis in the most dorsal lung region in $P0$ image. (b) The approximately same anatomic slice as (a) in $P5$ image. Notice that the fluid region (ROI in red rectangle) appears normal in $P5$ image.
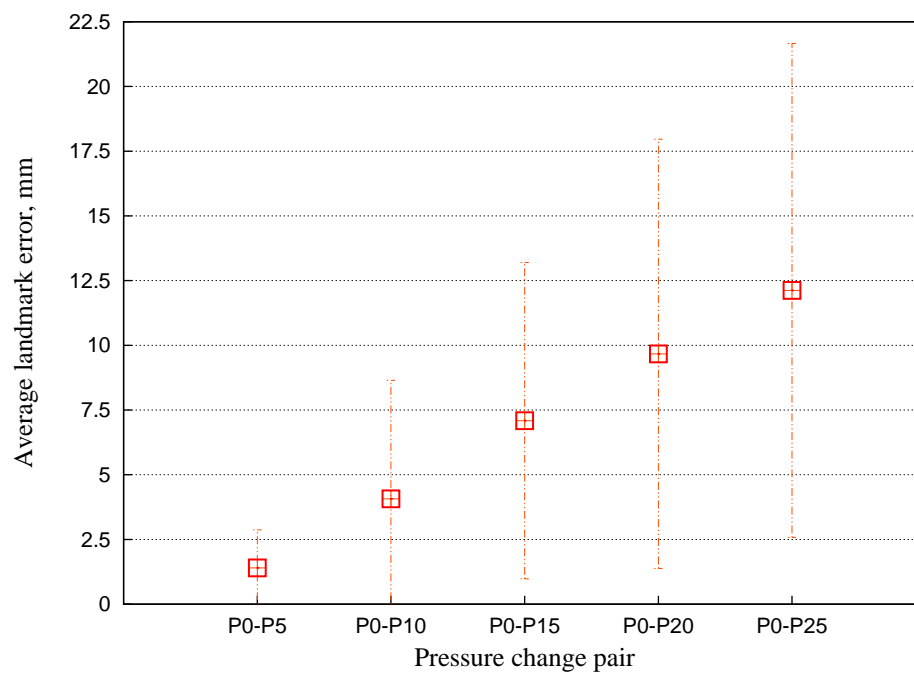
creasing pressure change pairs $P0$-$P5$, $P0$-$P10$, $P0$-$P15$, $P0$-$P20$, and $P0$-$P25$ starting from $P0$ for five sheep is shown in Figure 3.7(a). Figure 3.7(b) shows their mean landmark error averaged on five sheep. These data are shown in Table A.2.

The registration accuracy measured by predicting landmarks motion across increasing pressure change pairs $P10$-$P15$, $P10$-$P20$, and $P10$-$P25$ starting from $P10$ for five sheep is shown in Figure 3.8(a). Figure 3.8(b) shows their mean landmark error averaged on five sheep. These data are shown in Table A.3.

When the pressure change is increasing between images, the landmark error is also increasing, as shown in Figure 3.7 and Figure 3.8. This is caused by larger anatomic deformations between images in larger pressure change pair. The outlier sheep AS60150 showing much higher errors in Figure 3.7 is again caused by the low contrast in the $P0$ image. This is further confirmed in Figure 3.8 where the landmark
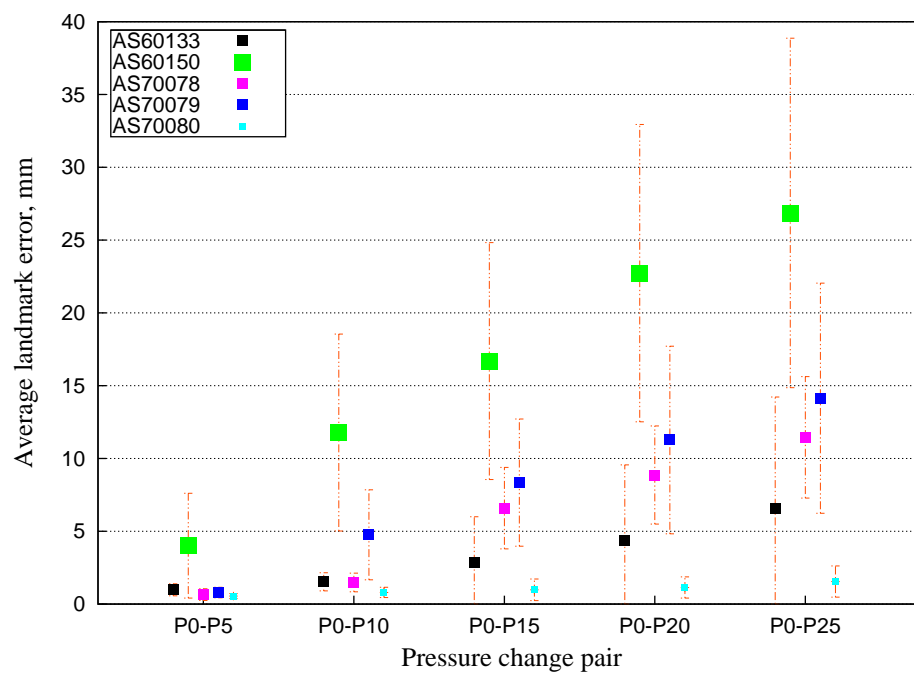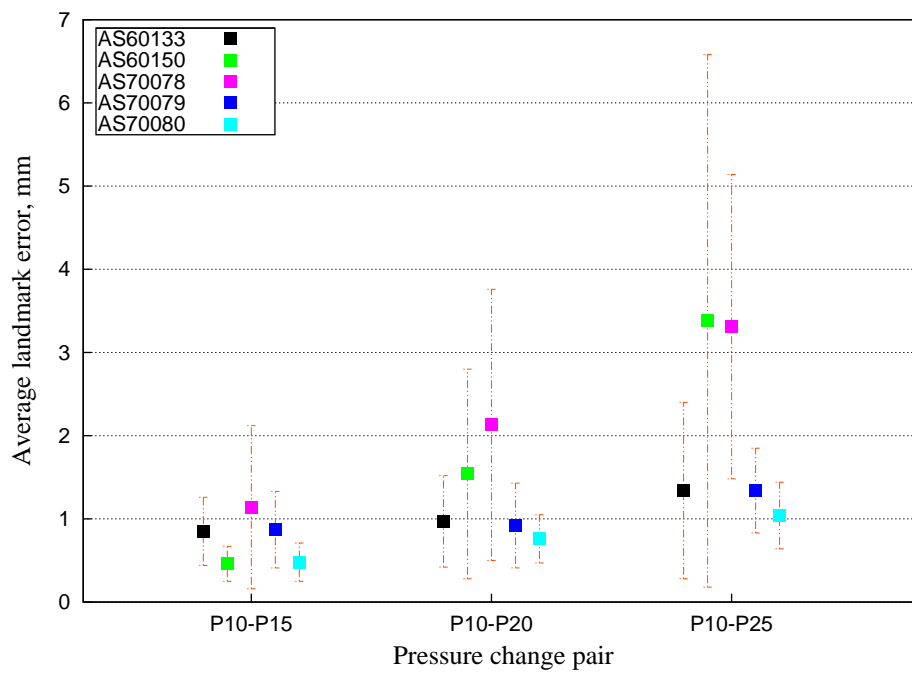
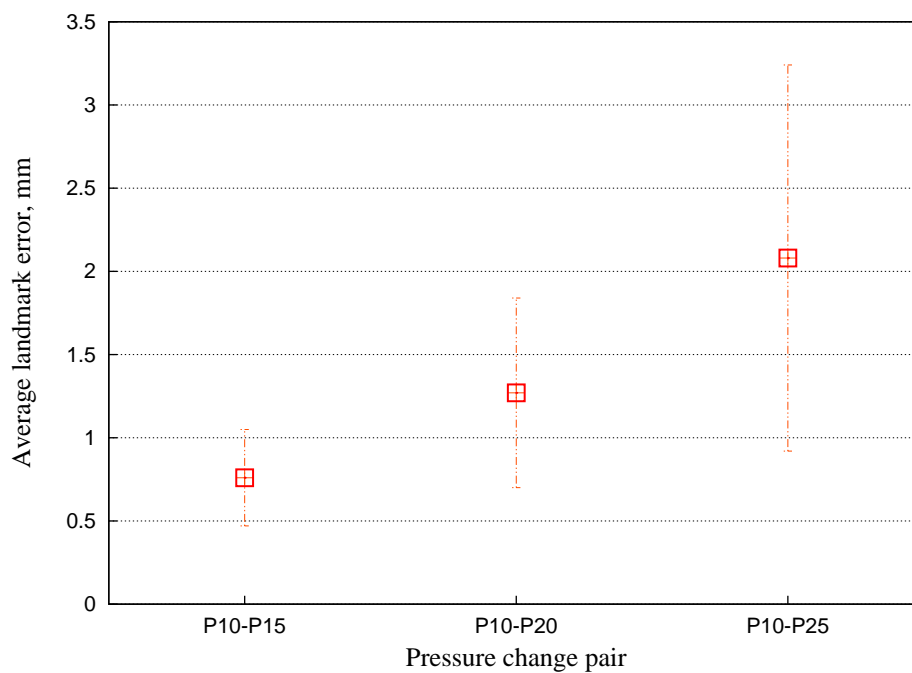Figure 3.7: Registration accuracy for increasing pressure change pairs starting from $P0$. (a) Mean landmark errors for each animal for each pressure change pair. (b) Mean landmark errors for each pressure change pair averaged across all five sheep.

(a)

(b)

Figure 3.8: Registration accuracy for increasing pressure change pairs starting from $P10$. (a) Mean landmark errors for each animal for each pressure change pair. (b) Mean landmark errors for each pressure change pair averaged across all five sheep.

error was calculated for increasing pressure change pairs starting from $P10$. In this case, all five sheep have less than 3.4 mm landmark error for the largest pressure change pair $P10$ to $P25$.

Note that the scale of average landmark error are different in Figure 3.7 and Figure 3.8. For the same pressure difference between images starting at $P0$ and $P10$, for example, $P0$ to $P15$ and $P10$ to $P25$, the average error over all five sheep from $P10$ to $P25$ (2 mm) is much lower than that from $P0$ to $P15$ (7 mm). This also proves that registration starting from higher pressure images is tend to be more accurate due to the decreased expansion magnitude and the improved contrast since the airway is opened up at higher pressure.

The registration process is sensitive to the magnitude of the tissue expansion. From Figure 3.7 we can see that when the pressure change is 10 cm H_2O, the average landmark error is around 2 mm excluding the sheep with atelectasis. However, when the pressure change is larger than 10 cm H_2O, the landmark error for some sheep increases dramatically. Also, by visualization of the registration results, we also found that the deformed images did not match well with the target images when pressure change exceeds 10 cm H_2O. Thus, The optimal sampling points during respiratory cycle for CT imaging is around 10 cm H_2O, which can lower the cost and radiation while guarantee the registration accuracy is acceptable.

3.2.2 Transitivity Error

For the two groups of transformations $P0$ to $P5$, $P5$ to $P10$, $P10$ to $P0$ and $P10$ to $P15$, $P15$ to $P20$, $P20$ to $P25$, $P25$ to $P0$, the average transitivity error over

Table 3.1: Transitivity error (mm)

Sheep	$P0 \rightarrow P5 \rightarrow P10 \rightarrow P0$	$P10 \rightarrow P15 \rightarrow P20 \rightarrow P25 \rightarrow P10$
AS60133	0.94	0.88
AS60150	3.29	2.04
AS70077	1.81	0.84
AS70078	0.93	1.60
AS70079	3.11	1.18
AS70080	0.34	0.52
mean error	1.74	1.18

the lung region for all six sheep is shown in the Table 3.1. The last row in the Table shows the average transitivity error for each group over six sheep.

From table 3.1, we notice that the average transitivity errors for both transformation groups are less than 2 mm, which is acceptable considering the large deformation resulted from the concatenation of those transformations. Note that the average transitivity error from $P10 \rightarrow P15 \rightarrow P20 \rightarrow P25 \rightarrow P10$ (1.18 mm) is even lower than that from $P0 \rightarrow P5 \rightarrow P10 \rightarrow P0$ (1.74 mm). This is caused by the larger deformation between lower pressure images and again the contrast improvement in higher pressure images. The big transitivity errors (more than 2mm) in AS60150 and AS70079 are resulted from the larger intensity difference (comparing with other sheep) in the dorsal lung region across different pressures. Since mean squared intensity difference is the similarity metric for our registration algorithm, large intensity difference will increase the difficulties of registration.

3.3   Assessment of Jacobian and Strain

After registration, Jacobian and strain measures were calculated based on the resulting displacement fields.

From the Jacobian map of transformations, we can estimate the local specific volume change for each pressure change pair. Figure 3.9 (a)-(e) show the local lung tissue specific volume change of a transverse section from sheep AS70078 across all five pressure change pairs. The resulting volume change map has few negative values. Figure 3.9 (f) shows the pressure change pair for each voxel when it experienced the largest expansion during the inflation phase.

From Figure 3.9 we noticed that lung tissue expands little from $P15$ to $P20$ and from $P20$ to $P25$. The first three pressure changes dominate the lung expansion. In addition, Figure 3.9 (f) shows that for this section, the superior half has most expansion from $P0$ to $P5$ while the inferior half has most expansion from $P10$ to $P15$.

Figure 3.10 shows the maps of Jacobian, maximal principal strain and aniso-tropic deformation index (ADI) on one transverse slice. Comparison between Jacobian and maximal principal strain together with the ADI map can reflect more lung tissue deformation information. For the ROI in black square which is near the aorta in the left lung, the Jacobian is big where the maximal principal strain is relatively small. This illustrates that this region experienced an isotropic expansion, shown as red in the ADI map (small ADI value approximately 1). For the ROI in red rectangle which is near the heart, the Jacobian is relatively small while its maximal principal strain
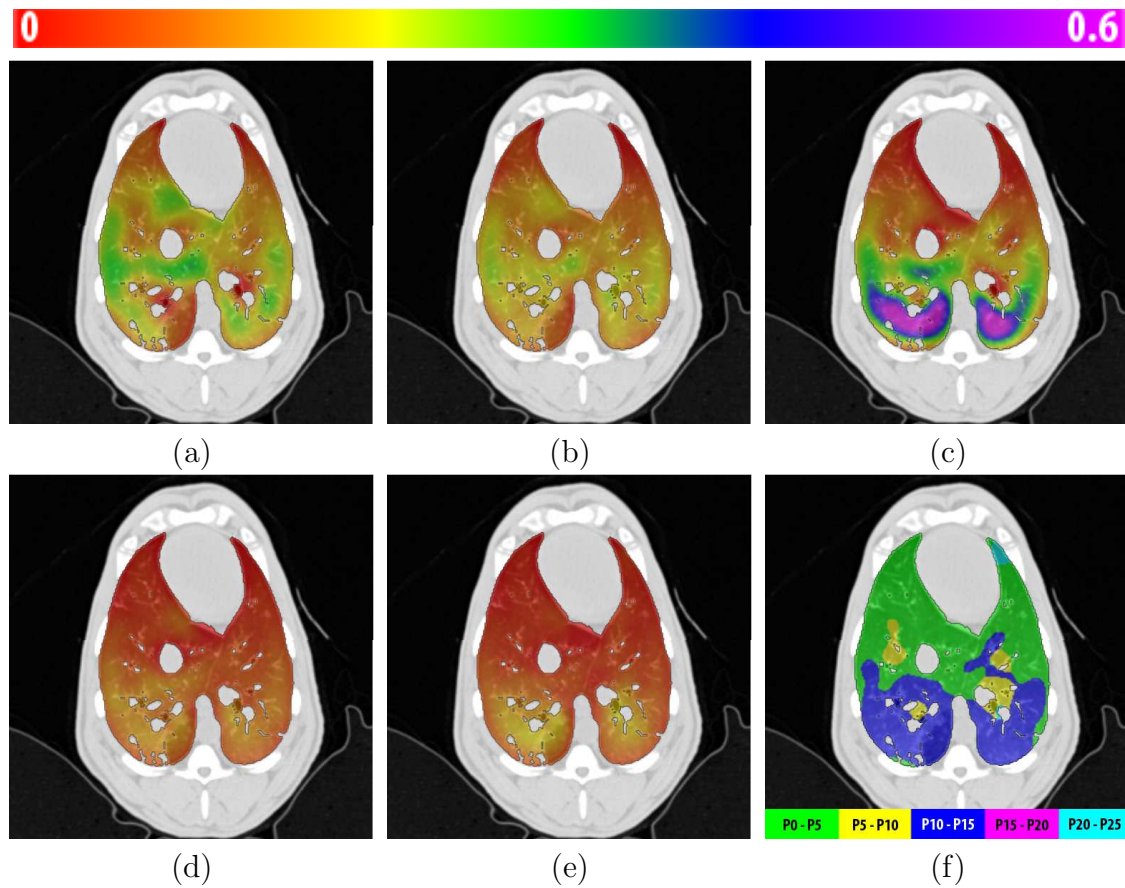
Figure 3.9: Local lung tissue specific volume change of a transverse section in (a) $P0$ to $P5$, (b) $P5$ to $P10$, (c) $P10$ to $P15$, (d) $P15$ to $P20$, and (e) $P20$ to $P25$ pressure change pairs for sheep AS70078. (f) shows the pressure change pair for each voxel when it experienced the largest expansion.

is large. This illustrates that region experienced an anisotropic expansion, shown as purple in the ADI map (larger ADI value approximately 2). This anisotropic expansion may be caused by the presence of the heart.

| 0.95 | 1.73 | 0.05 | 0.67 | 1.05 | 2.08 |

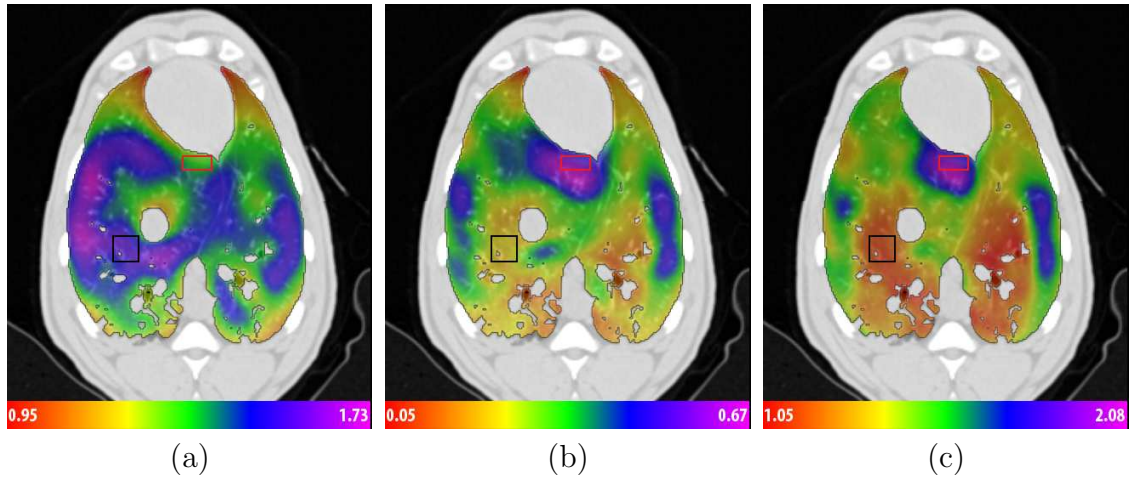| (a) | (b) | (c) |

Figure 3.10: Lung expansion measures resulted from registration. (a) Jacobian, (b) maximal principal strain, and (c) anisotropic deformation index on a transverse slice when lung expanded from $P0$ to $P10$ for sheep AS70078.

After applying strain tensor on the transformation, the directions along which there is only linear strain (stretch or compression) for local lung tissue were also estimated using SVD analysis. Figure 3.11 illustrates the maximal principal direction, maximal principal strain, and Jacobian together on a transverse slice and a coronal slice. It enable us to get more details of the lung tissue expansion instead of just knowing the expansion ratio from Jacobian.
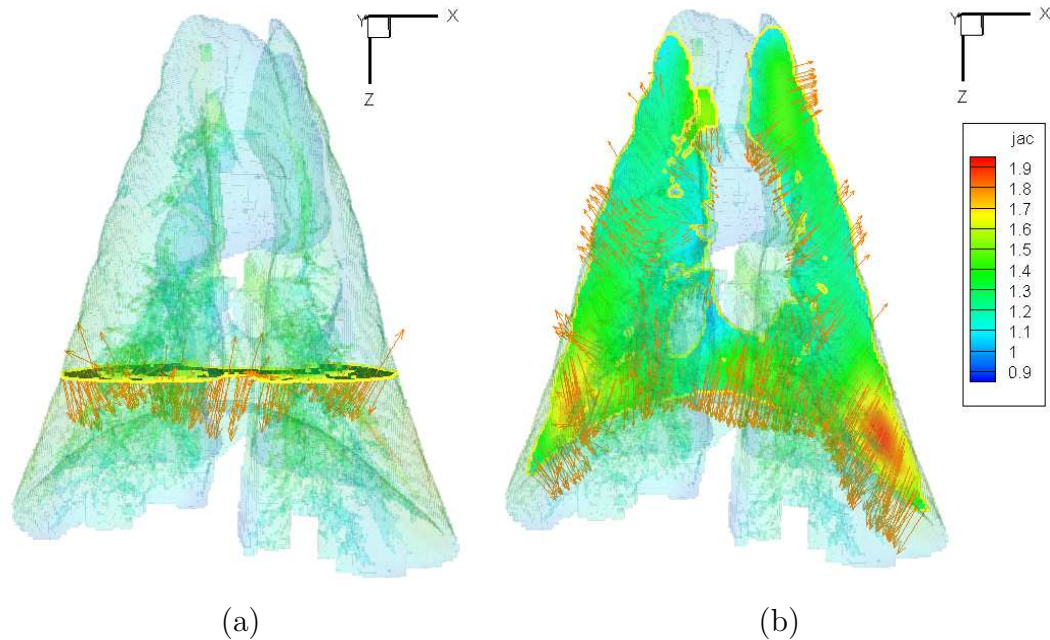
Figure 3.11: Maximal principal direction of $P0$ to $P10$ transformation on (a) a transverse slice and (b) a coronal slice for sheep AS70078. The vector magnitude represents the maximal principal strain, and the colored contour expresses the Jacobian.

3.4   Comparison Experiments

From the registration results and Xe-CT analysis, Jacobian, intensity-based volume change and specific ventilation were calculated. Color-coded maps of the three parameters at approximately the same anatomic location for sheep AS70078 are shown in Figure 3.12. From the three maps, a relationship between the three measurements can be observed. There are similar ventral-dorsal gradients in these maps, which is consistent with known physiology that the more dependent region of lung has more ventilation. The sheep is at the supine position, then the more dependent region of lung is the dorsal region since it is closest to the direction of the force of gravity. Thus, there are more ventilation and expansion in the dorsal region.
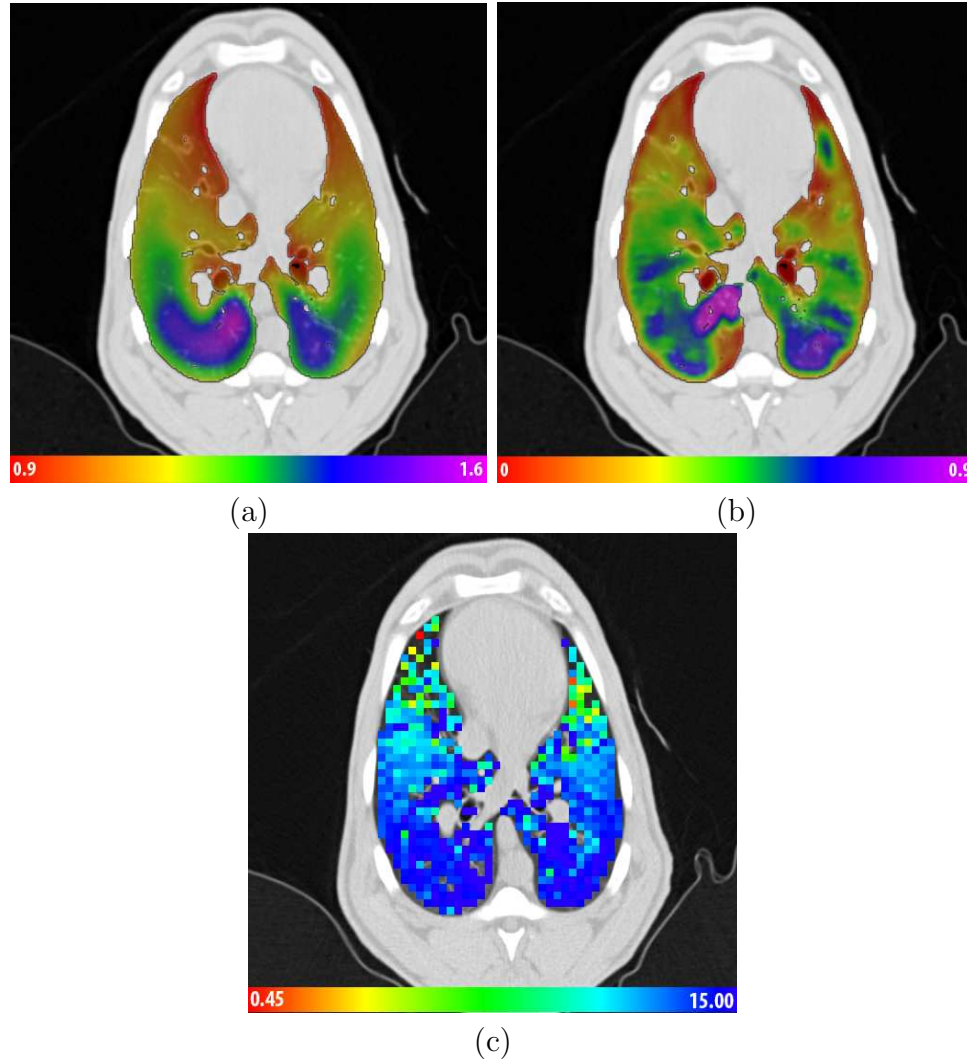
Figure 3.12: Color-coded maps showing (a) Jacobian of the registration transformation, (b) intensity-based volume change computed from the $P10 - P15$ image pair, and (c) specific ventilation (1/min) for approximately the same anatomic slice computed from Xe-CT at $P10$ of sheep AS70078. Note that the physical units and color scales are different for three images.

For five sheep, the average sV from Xe-CT at $P0$, and the average Jacobian
and intensity-based regional volume change for all five 5 cm H_2O pressure change
pairs vs. lung height were calculated and shown in Appendix C. These data for
sheep AS70078 is shown in Figure 3.13 here. It shows the ventral-dorsal gradients in
the measures of average sV, Jacobian, and intensity-based regional volume change. In
addition, Figure 3.13(b)-(c) show that the lung at lower pressures has more expansion
on average, which also compares well with known physiology. From Figure 3.13(b)-
(c), we noticed there is a jump in $P10$ to $P15$ curve at the dorsal region. This
corresponds to the pattern shown in Figure 3.9 that dorsal region experiences large
expansion from $P10$ to $P15$. It implies that for sheep AS70078, 10 cm H_2O is a
critical pressure for the airway in dorsal region to open up.
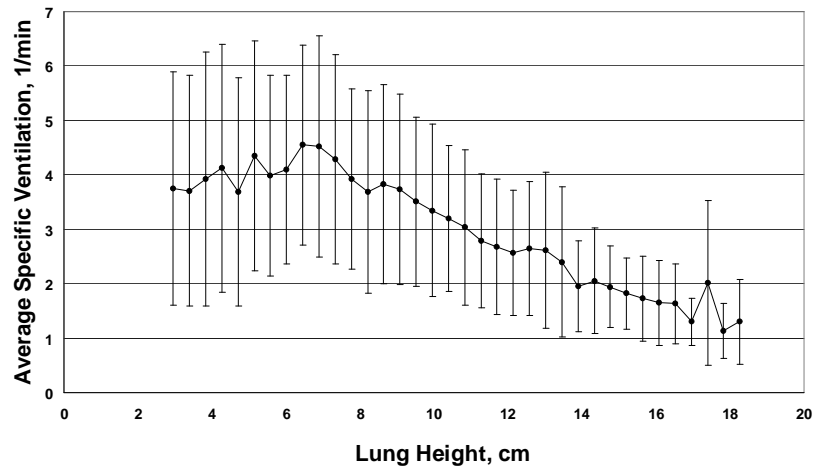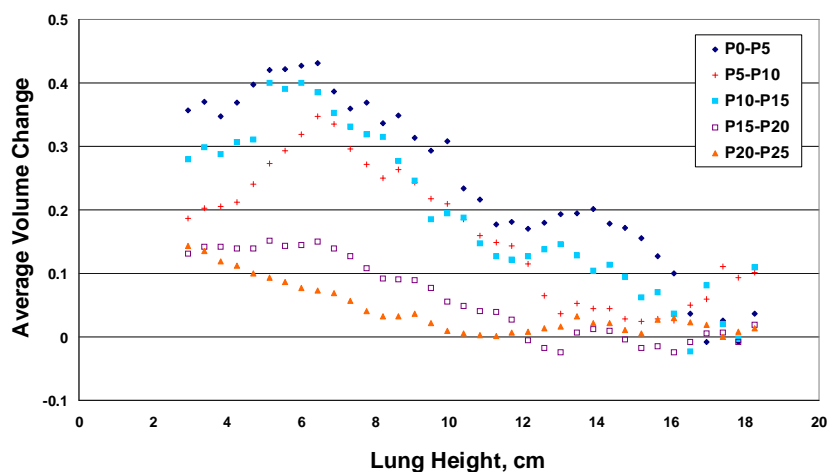

(a)

Figure 3.13: Example of sV, Jacobian and intensity-based regional volume change
measurements vs. lung height for sheep AS70078. (a) Average $\pm$ standard deviation
of sV vs. lung height; (b) average Jacobian for all pressure pairs vs. lung height; and
(c) intensity-based regional volume change for all pressure pairs vs. lung height.
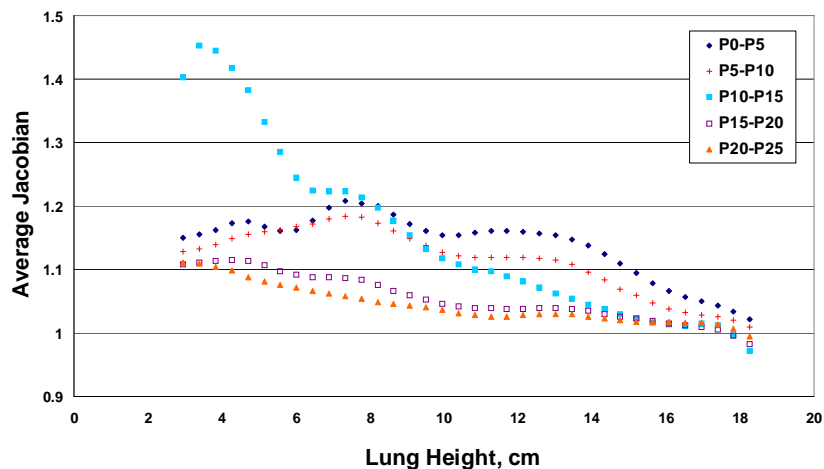
(b)

(c)

Figure 3.13 continued.

From Figure 3.13, it is reasonable to make a guess that there exists a linear relationship between sV and other two measures derived from registration. Take the Jacobian and sV as an example, in order to compare the two estimates, an average Jacobian vs. average sV scatter plot was made and a linear regression line was used to fit on the scatter data. Figure 3.14 shows the average Jacobian of $P5$ to $P10$

transformation vs. average sV at $P0$ in sheep AS70078. The intensity-based regional volume change was compared with sV in the same way.
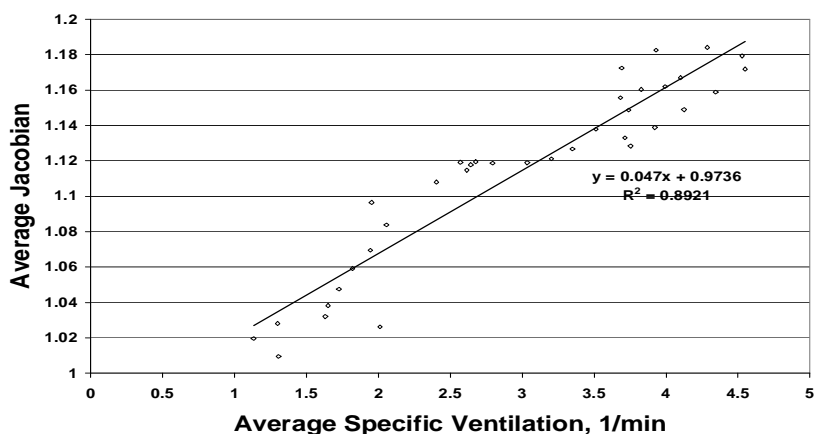

Figure 3.14: Scatter plots of average Jacobian over average sV for the $P5$ to $P10$ transformation for sheep AS70078. Linear regression line and the squared correlation coefficients are shown in the chart.

For five sheep, the correlation coefficients r were calculated from the linear regression of the measures resulted from registration and sV obtained at $P0$ for each 5 cm H_2O pressure change pair. The correlation coefficients for each comparison, each pressure change pair and each sheep are shown in Figure 3.15. These data and average correlation coefficient for each pressure change pair over five sheep are shown in Table B.1 and Table B.2.

Xe-CT images at $P10$ are available for four sheep. Thus, the correlation of the average Jacobian, the intensity-based regional volume change for $P10$ to $P15$, $P15$ to $P20$, $P20$ to $P25$ image pairs with the average sV from Xe-CT at $P10$ were evaluated
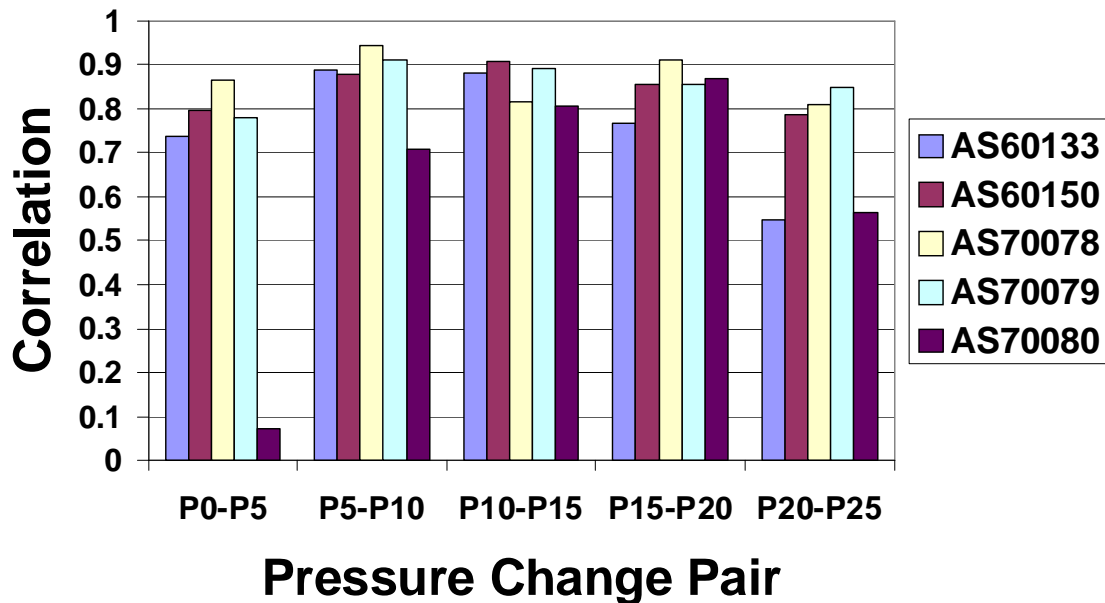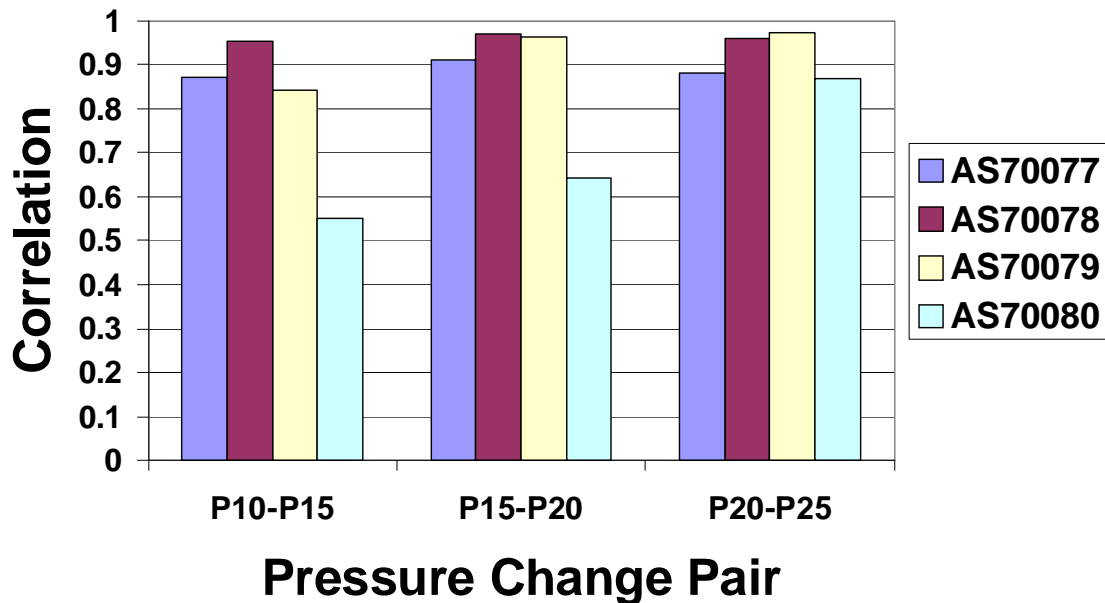
(a)
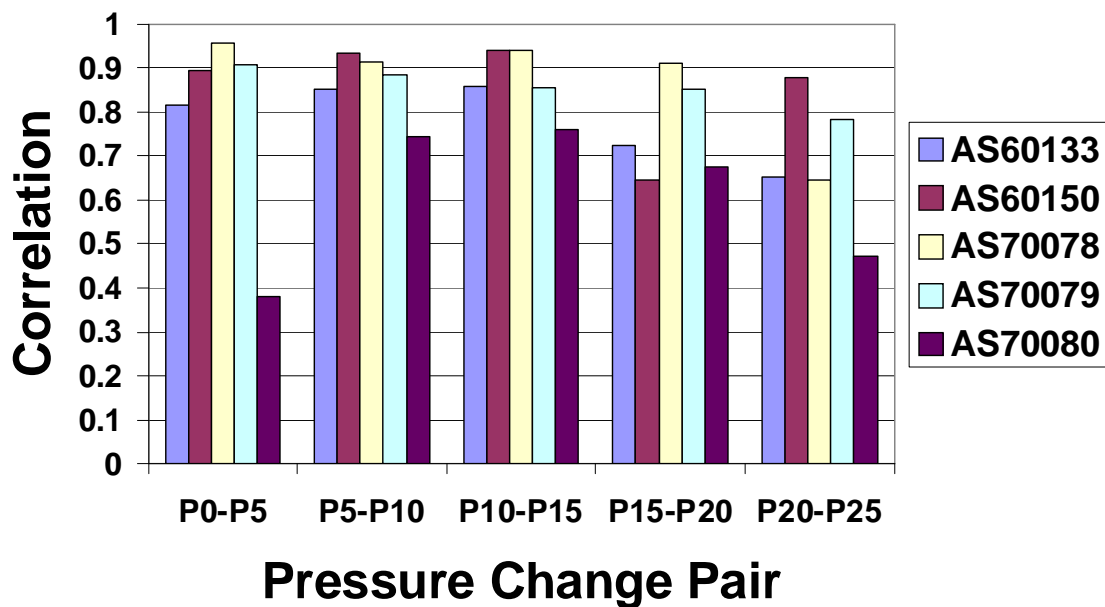
(b)

Figure 3.15: Correlation coefficients r from the linear regression of (a) Jacobian and sV at $P0$, and (b) intensity-based regional volume change and sV at $P0$ for each 5 cm H_2O pressure change pair starting from $P0$ and for five sheep.

respectively using the same method described above. The correlation coefficients for each comparison, each pressure change pair and each sheep are shown in Figure 3.16. These data and average correlation coefficient for each pressure change pair over four sheep are shown in Table B.3 and Table B.4.

Figure 3.15 and Figure 3.16 show there is a reasonably strong linear relationship between sV analysis from Xe-CT studies and the regional expansion from registrations of CT images over a wide range of pressures. For analysis starting from $P0$, the correlations for image pairs $P5$ to $P10$ and $P10$ to $P15$ are stably higher (around 0.87) than other pairs across five sheep and across two comparison experiments. For analysis starting from $P10$, correlations for all image pairs are stably high (larger than 0.84) for three sheep of four.

The outlier sheep AS70080 has extremely low correlation coefficient from $P0$ to $P5$ in Figure 3.15 and relatively lower correlation coefficient in $P10$ to $P15$ and $P15$ to $P20$ pairs in Figure 3.16. Further inspection revealed that this sheep also had severe atelectasis in the dorsal region across all six pressures. This fluid region in $P10$ image is shown in Figure 3.17.

However, AS70080 has very small landmark error. The reason is that those selected landmarks are distributed in the central region of lung, and no landmark is located in the fluid region. The transitivity errors for AS70080 are also small since the atelectasis exists in all six images of increasing pressures. In order to check the the registration accuracy in the dorsal region when atelectasis exists, it is necessary to have widely distributed landmarks and other evaluation methods.

(a)
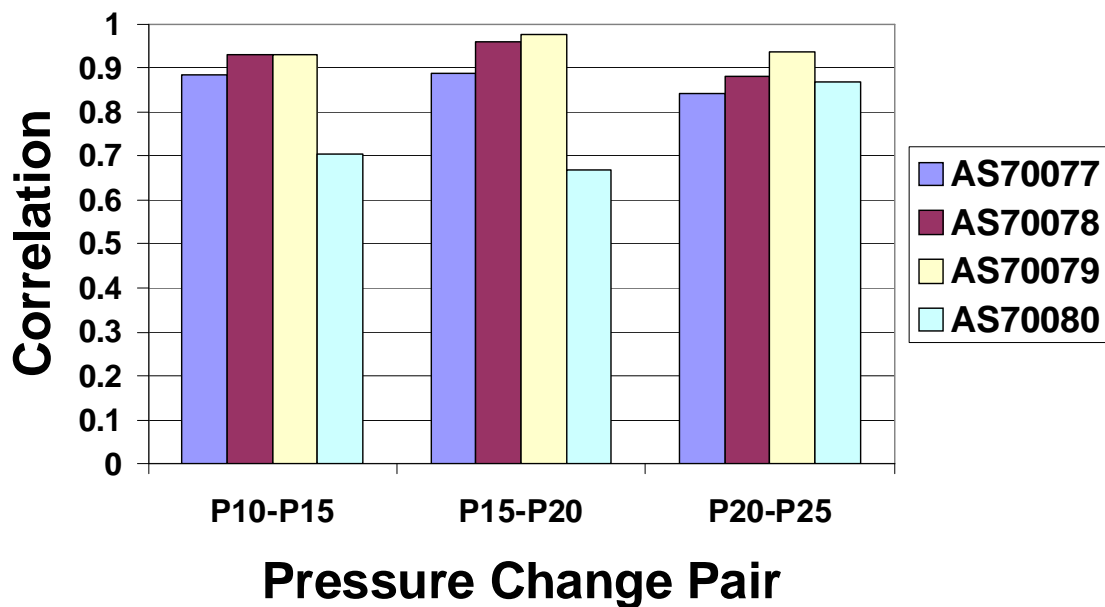
(b)

Figure 3.16: Correlation coefficients r from the linear regression of (a) Jacobian and sV at $P10$, and (b) intensity-based regional volume change and sV at $P10$ for each 5 cm H_2O pressure change pair starting from $P10$ and for four sheep.
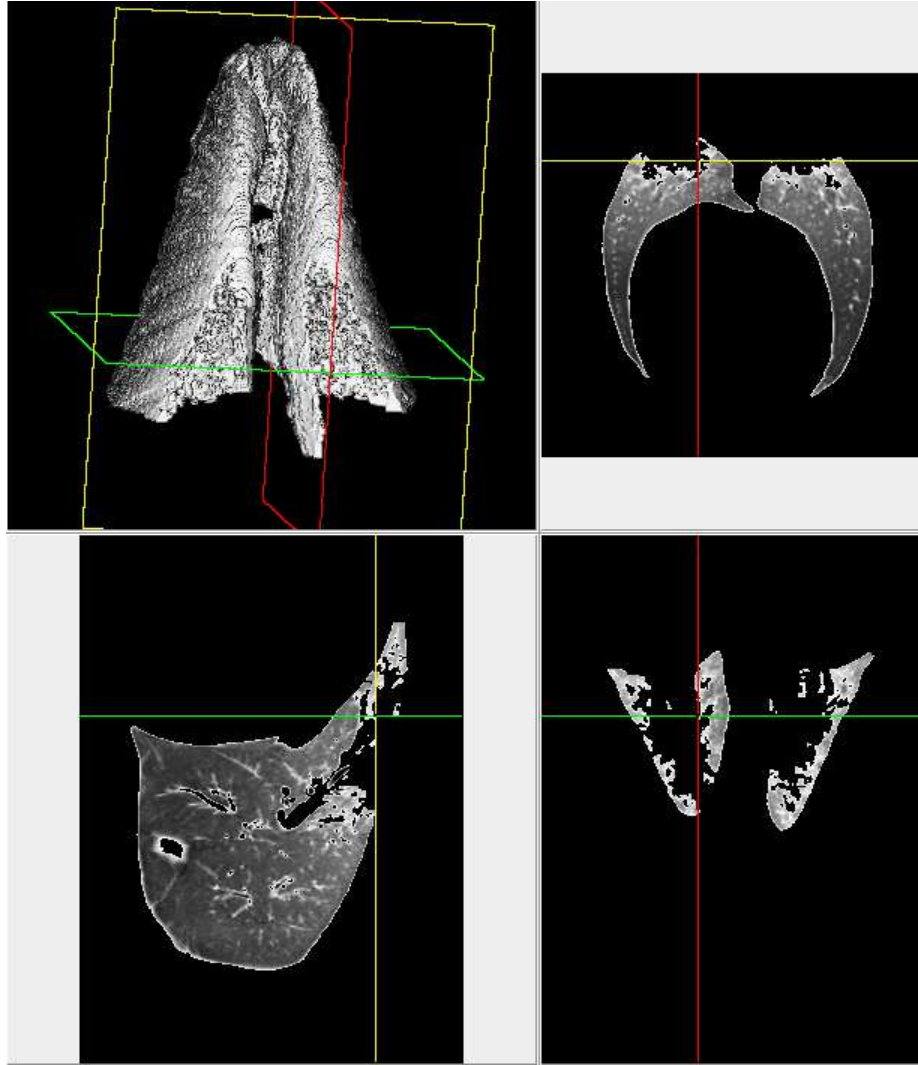
Figure 3.17: Atelectasis in sheep AS70080 in $P10$ image.

3.5   Experiment using MI Registration

Registrations were done on $P10$ to $P15$, $P15$ to $P20$ and $P20$ to $P25$ pairs using a mutual information (MI) similarity cost function based SICLE algorithm. MI registration runs 5 to 10 minutes longer than MSQ registration. Figure 3.18 illustrates the joint histograms of the image pairs before and after MI registration. Notice that the spread of the joint histogram is much less after registration.
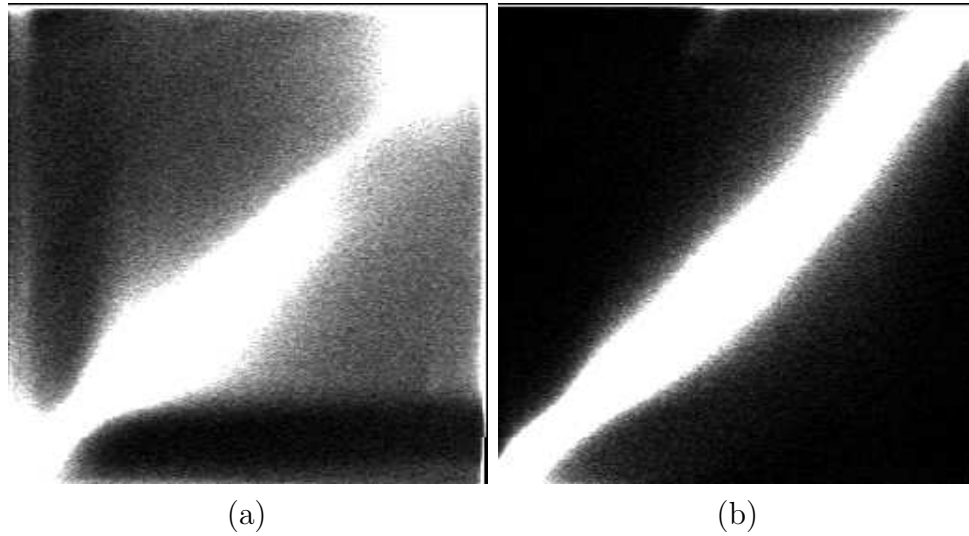
Figure 3.18: Joint histogram of (a) $P10$ and $P15$ before registration, and (b) deformed $P10$ and $P15$ after registration for sheep AS70079.

The registration accuracy measured by predicting landmarks motion across three 5 cm H_2O pressure change pairs for five sheep is shown in Figure 3.19(a). Figure 3.19(b) shows their mean landmark error averaged on five sheep. These data are shown in Table A.4. The landmark errors are within 1 mm, which are acceptable since those errors are in the sub-voxel level.

The comparison between Jacobian, intensity-based regional volume change estimated from the resulting displacement fields with sV from Xe-CT at $P10$ were also analyzed for four sheep which have $P10$ Xe-CT data. The correlation coefficients for each comparison and each sheep at $P10$ to $P15$, $P15$ to $P20$ and $P20$ to $P25$ pressure change pairs are shown in Figure 3.20. These data and average correlation coefficient for each pressure change pair over four sheep are shown in Table B.5 and Table B.6. These correlation coefficients are quite similar with those generated from registra-
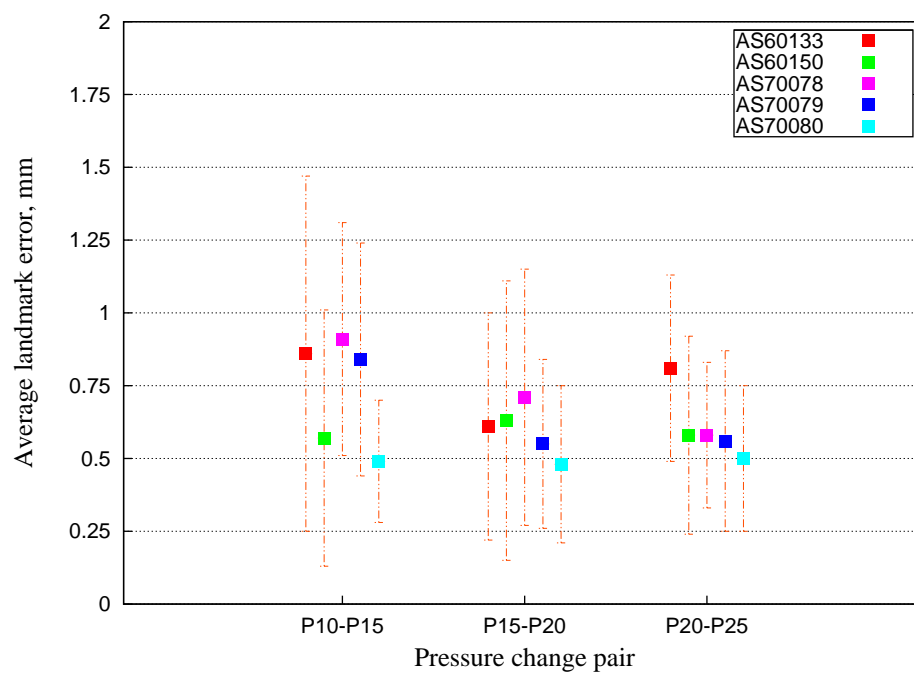
(a)
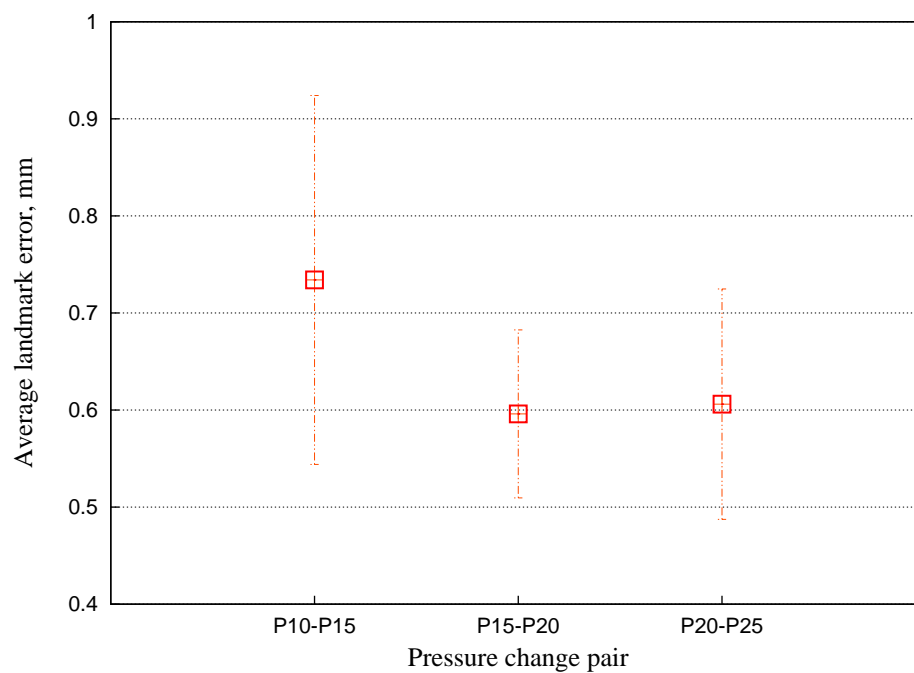
(b)

Figure 3.19: MI registration accuracy for three 5 cm H_2O pressure change pairs. (a) Mean landmark errors for each animal for each pressure change pair. (b) Mean landmark errors for each pressure change pair averaged across all five sheep.
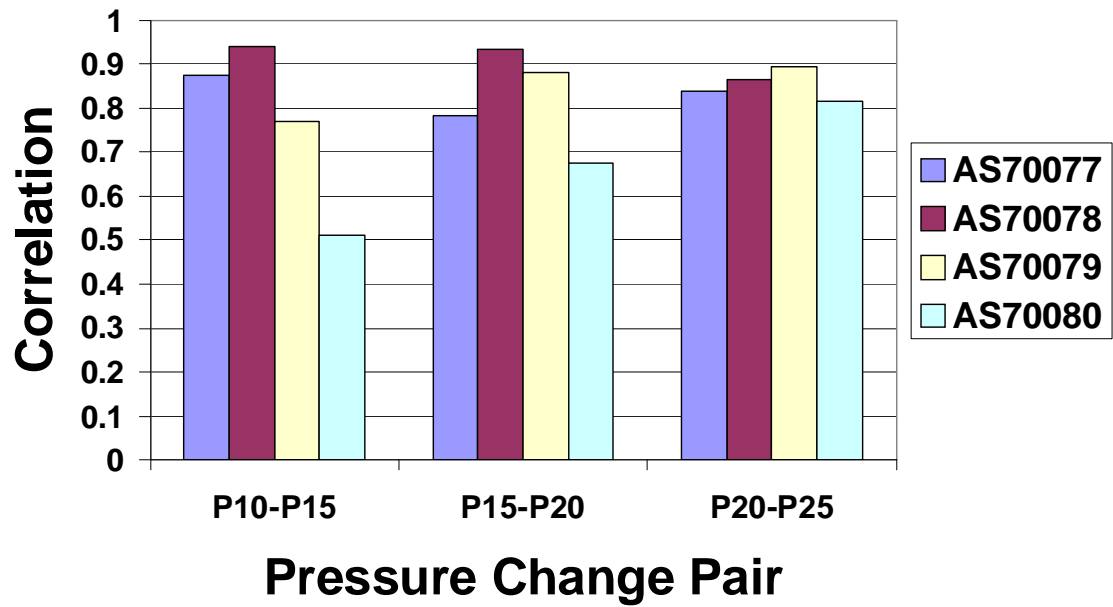
(a)
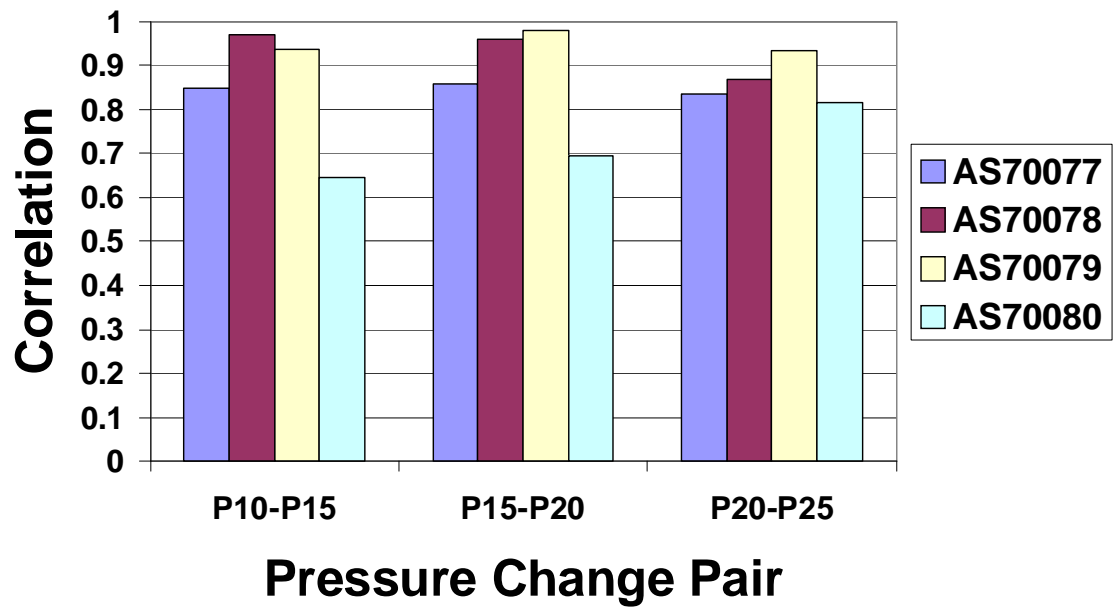
(b)

Figure 3.20: Correlation coefficients r from the linear regression of (a) Jacobian and sV at $P10$ (b) intensity-based regional volume change and sV at $P10$ for each 5 cm H_2O pressure change pair starting from $P10$ and for four sheep. The Jacobian and intensity-based regional volume change are estimated from mutual information driven registration.

tion driven by minimizing mean squared intensity difference. This proves that the grayscale mapping to emphasize the tissue-vessel and tissue-chest wall boundaries is useful for later registration, and the intensity difference based registration is effective in this application.

CHAPTER 4
DISCUSSION

In this project, most of the work is based on registration. Thus, the registration accuracy evaluation is necessary and important. Tracking landmark errors and transitivity errors are two ways to evaluate the accuracy, but they are far from enough. Further investigation of the registration accuracy is needed, such as tracking known displacements in a phantom, assessment of anatomic overlap, and comparison with known synthetic deformations. One existing problem is that the lung tissues near large vessels should have large deformation physiologically, however, this phenomenon does not show in the Jacobian map. This may be caused by the smooth constraint on displacement fields during the registration process. Whether this smooth constraint is suitable for the lung deformation is still unknown and need to be further investigated. In addition, the registration tends to be inaccurate near regions of lung where the airways open up at higher pressures. Developing a robust registration scheme to deal with such case is also necessary in order to be applied on the patients who has atelectasis or edema.

Currently, mutual information registration algorithm is optimized using gradient descent. However, this optimization method can get stuck in local minima with a mutual information cost function. In the future, we will need to investigate using other optimization methods.

For all the comparison experiments, sV were used to compare with measures

estimated from CT image pair with 5 cm H_2O pressure change. We can compare sV with registration results from larger step pressure change pairs and evaluate the correlation in order to find the image pair which correlates sV best (stably higher than others).

We are currently estimating the lung expansion in the supine position. It is interesting to investigate the lung contraction in the exhalation process. Lung motion in the prone position also need to be analyzed.

This work can be extended to the treatment of lobar anatomy by segmenting the lobes of the lung and registering them separately. This will help accommodate the lobar slippage and rotations that are observed.

CHAPTER 5
CONCLUSION

This thesis work has illustrated a registration-based technique for estimating local lung tissue expansion during respiratory cycle from multiple respiratory-gated CT images. The degree of expansion is estimated using Jacobian and ventilation theory, while the stretching direction and magnitude are revealed using strain tensor. There measures are all generated from the displacement fields estimated in registration process.

The registration accuracy was evaluated by tracking landmarks motion and computing transitivity error. The average landmark errors are within 1.5 mm except an outlier at the lowest pressure change pair. The average transitivity errors are within 1.8 mm.

The Jacobian, ventilation and sV maps all show the ventral-dorsal gradient. The comparison between the measures of regional lung expansion estimated by registration and the regional ventilation from Xe-CT analysis shows strong correlation. This comparison result gives confidence that image registration can track the lung motions and be used to build the lung expansion model.

Registration starting from images higher than 10 cm H_2O pressure can results more accurate transformations, and more stable correlations between the measures from registration and sV estimated from Xe-CT image at $P10$.

The ventilation analysis based on Xe-CT imaging is only available to a small

number of research groups due to its high imaging cost, limited spatial coverage and limited spatial resolution. Comparing with Xe-CT analysis, the registration-based specific volume change and strain analysis of lung expansion can provide high-resolution map and directional information for the entire lung using just two volumetric images acquired at different lung volumes. Therefore, using the technique described in this thesis work, we are able to get a more detailed and more complete assessment of lung tissue expansion at lower cost.

APPENDIX A
LANDMARK ERROR

Table A.1: Landmark error for 5 cm H_2O pressure change pairs (mm)

Sheep	$P0 \rightarrow P5$	$P5 \rightarrow P10$	$P10 \rightarrow P15$	$P15 \rightarrow P20$	$P20 \rightarrow P25$
AS60133	0.98	1.09	0.85	0.59	0.79
AS60150	4.01	1.46	0.46	0.52	0.51
AS70078	0.65	1.00	1.14	0.73	0.57
AS70079	0.79	0.70	0.87	0.54	0.55
AS70080	0.55	0.56	0.48	0.49	0.52
Ave. error	1.40	0.96	0.76	0.57	0.59

Table A.2: Landmark error for increasing pressure change pairs from $P0$ (mm)

Sheep	$P0 \rightarrow P5$	$P0 \rightarrow P10$	$P0 \rightarrow P15$	$P0 \rightarrow P20$	$P0 \rightarrow P25$
AS60133	0.98	1.53	2.83	4.37	6.58
AS60150	4.01	11.78	16.69	22.73	26.86
AS70078	0.65	1.48	6.59	8.86	11.45
AS70079	0.79	4.76	8.34	11.27	14.14
AS70080	0.55	0.80	0.98	1.14	1.55
Ave. error	1.40	4.07	7.09	9.67	12.12

Table A.3: Landmark error for increasing pressure change pairs from $P10$ (mm)

Sheep	$P10 \rightarrow P15$	$P10 \rightarrow P20$	$P10 \rightarrow P25$
AS60133	0.85	0.97	1.34
AS60150	0.46	1.54	3.38
AS70078	1.14	2.13	3.31
AS70079	0.87	0.92	1.34
AS70080	0.48	0.76	1.04
Ave. error	0.76	1.27	2.08

Table A.4: MI registration resulting landmark error for 5 cm H_2O pressure change pairs from $P10$ (mm)

Sheep	$P10 \rightarrow P15$	$P15 \rightarrow P20$	$P20 \rightarrow P25$
AS60133	0.86	0.61	0.81
AS60150	0.57	0.63	0.58
AS70078	0.91	0.71	0.58
AS70079	0.84	0.55	0.56
AS70080	0.49	0.48	0.50
Ave. error	0.73	0.60	0.61

APPENDIX B
CORRELATION COEFFICIENTS

Table B.1: Correlation coefficients (CC) of Jacobian with sV at $P0$

Sheep	$P0 \rightarrow P5$	$P5 \rightarrow P10$	$P10 \rightarrow P15$	$P15 \rightarrow P20$	$P20 \rightarrow P25$
AS60133	0.74	0.89	0.88	0.77	0.55
AS60150	0.80	0.88	0.91	0.86	0.79
AS70078	0.87	0.94	0.82	0.91	0.81
AS70079	0.78	0.91	0.89	0.85	0.85
AS70080	0.07	0.71	0.81	0.87	0.56
Ave. CC	0.65	0.87	0.86	0.85	0.71

Table B.2: Correlation coefficients (CC) of intensity-based regional volume change with sV at $P0$

Sheep	$P0 \rightarrow P5$	$P5 \rightarrow P10$	$P10 \rightarrow P15$	$P15 \rightarrow P20$	$P20 \rightarrow P25$
AS60133	0.81	0.85	0.86	0.72	0.65
AS60150	0.89	0.93	0.94	0.64	0.88
AS70078	0.95	0.91	0.94	0.91	0.65
AS70079	0.91	0.89	0.85	0.85	0.78
AS70080	0.38	0.74	0.76	0.68	0.47
Ave. CC	0.79	0.87	0.87	0.76	0.69

Table B.3: Correlation coefficients (CC) of Jacobian with sV at $P10$

Sheep	$P10 \rightarrow P15$	$P15 \rightarrow P20$	$P20 \rightarrow P25$
AS70077	0.87	0.91	0.88
AS70078	0.95	0.97	0.96
AS70079	0.84	0.96	0.97
AS70080	0.55	0.64	0.87
Ave. CC	0.80	0.87	0.92

Table B.4: Correlation coefficients (CC) of intensity-based regional volume change with sV at $P10$

Sheep	$P10 \rightarrow P15$	$P15 \rightarrow P20$	$P20 \rightarrow P25$
AS70077	0.88	0.89	0.84
AS70078	0.93	0.96	0.88
AS70079	0.93	0.98	0.94
AS70080	0.71	0.67	0.87
Ave. CC	0.86	0.87	0.88

Table B.5: MI registration resulted correlation coefficients (CC) of Jacobian with sV at $P10$

Sheep	$P10 \rightarrow P15$	$P15 \rightarrow P20$	$P20 \rightarrow P25$
AS70077	0.88	0.78	0.84
AS70078	0.94	0.93	0.86
AS70079	0.77	0.88	0.90
AS70080	0.51	0.68	0.81
Ave. CC	0.77	0.82	0.85

Table B.6: MI registration resulted correlation coefficients (CC) of intensity-based regional volume change with sV at $P10$

| Sheep	$P10 \rightarrow P15$	$P15 \rightarrow P20$	$P20 \rightarrow P25$
AS70077	0.85	0.86	0.83
AS70078	0.97	0.96	0.87
AS70079	0.94	0.98	0.93
AS70080	0.65	0.70	0.81
Ave. CC	0.85	0.87	0.86

APPENDIX C
FIGURES OF ESTIMATES VS. LUNG HEIGHT
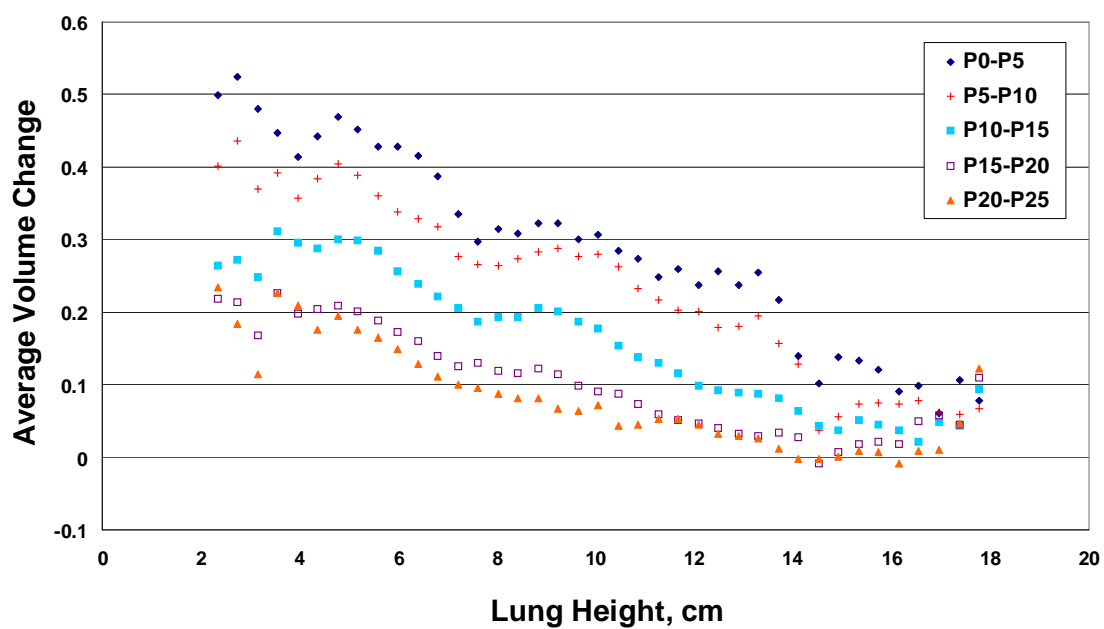
C.1   Sheep AS60133
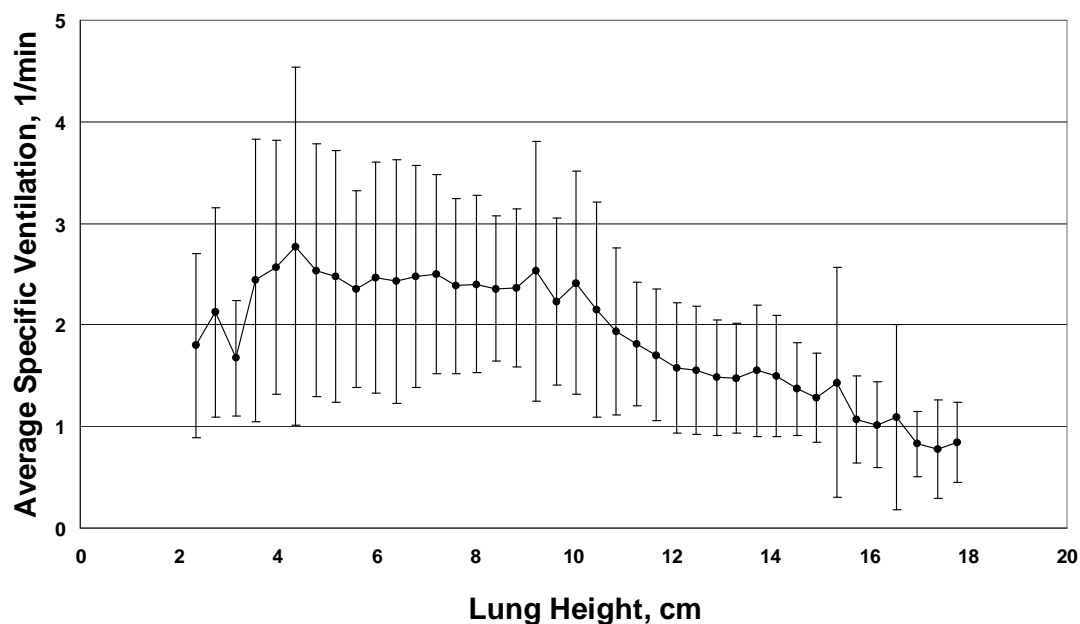
(a)

Figure C.1: The sV, Jacobian and intensity-based regional volume change measurements vs. lung height for sheep AS60133. (a) Average $\pm$ standard deviation of sV analyzed from Xe-CT at $P0$ vs. lung height; (b) average Jacobian for all 5 cm pressure change pairs vs. lung height; and (c) intensity-based regional volume change for all 5 cm pressure change pairs vs. lung height.
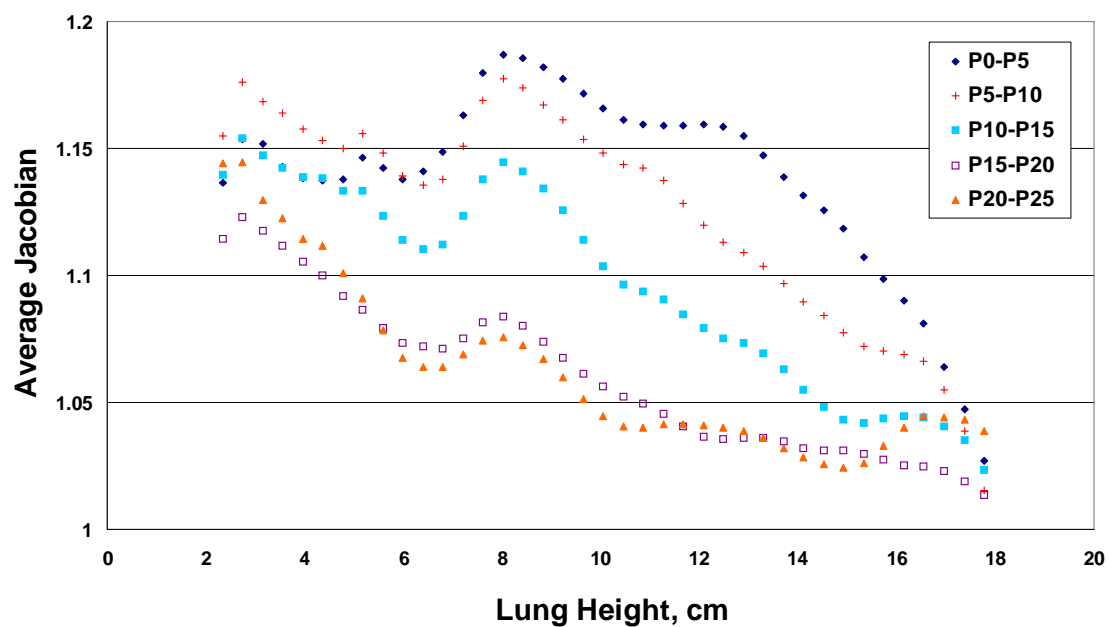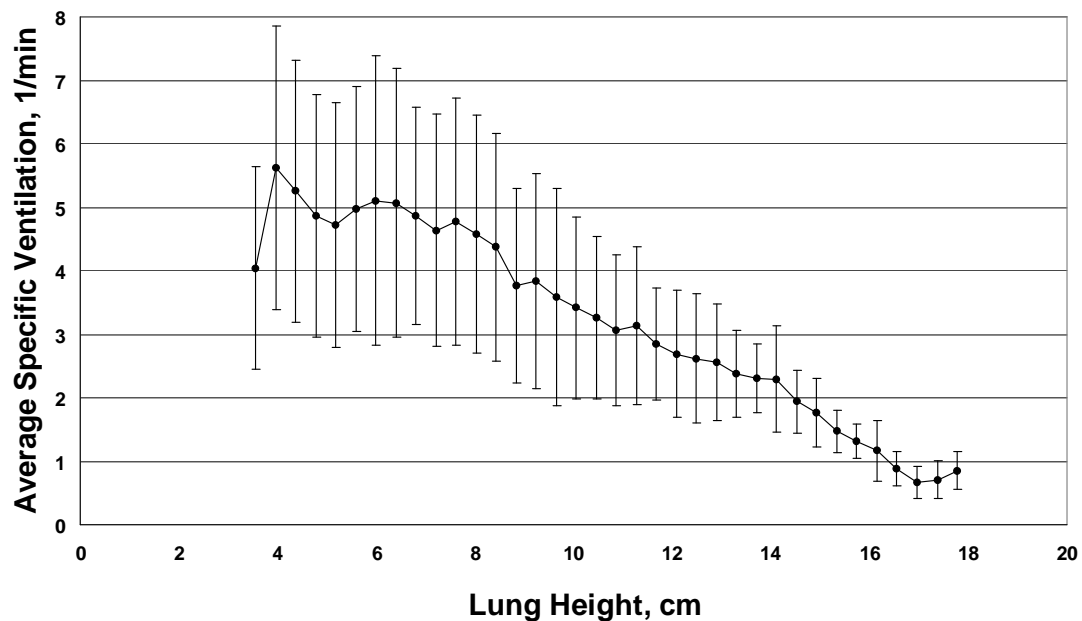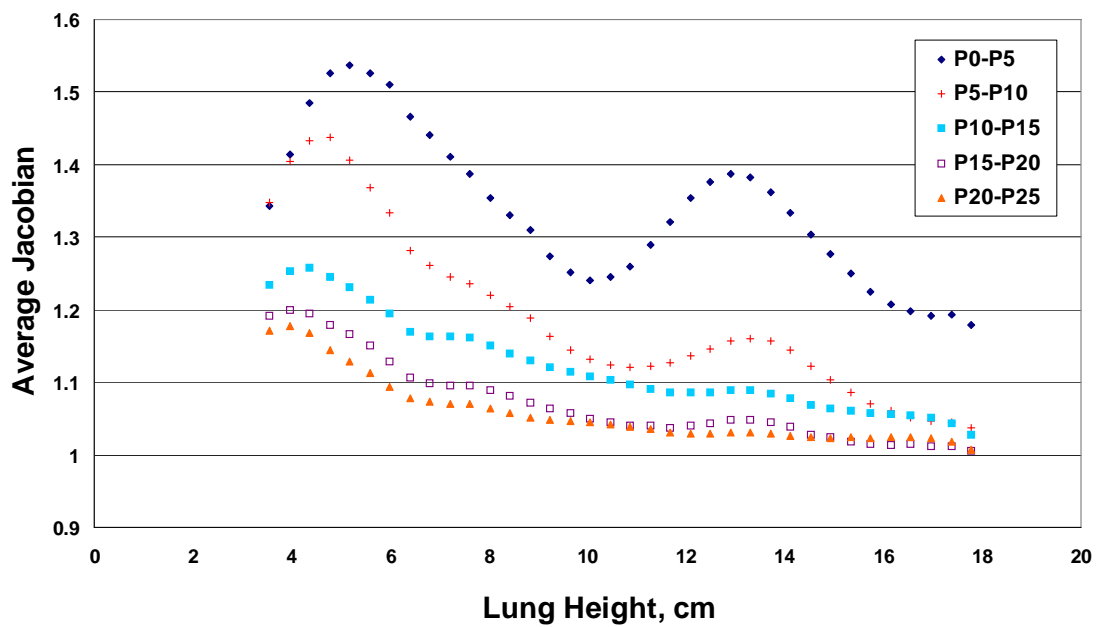
(b)

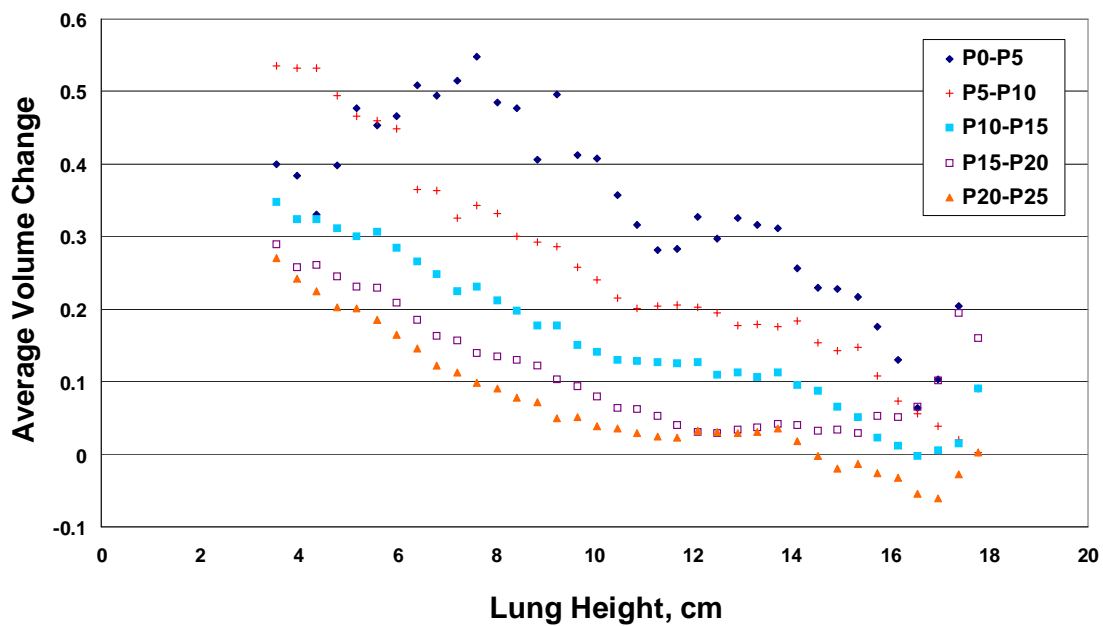

(c)

Figure C.1 continued.

C.2 Sheep AS60150

(a)

Figure C.2: The sV, Jacobian and intensity-based regional volume change measurements vs. lung height for sheep AS60150. (a) Average ± standard deviation of sV analyzed from Xe-CT at $P0$ vs. lung height; (b) average Jacobian for all 5 cm pressure change pairs vs. lung height; and (c) intensity-based regional volume change for all 5 cm pressure change pairs vs. lung height.
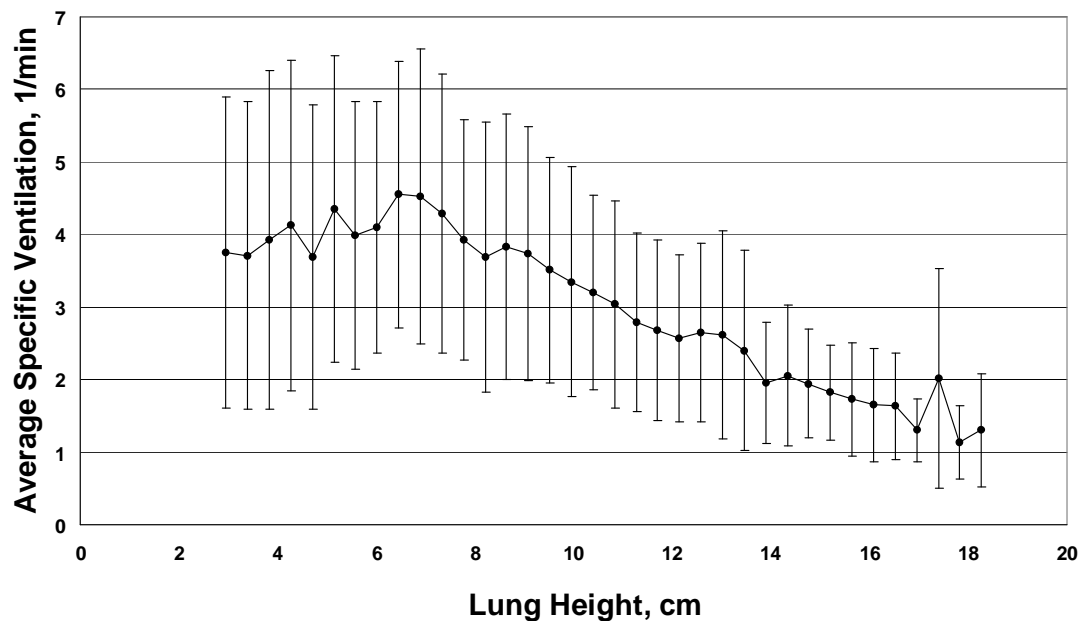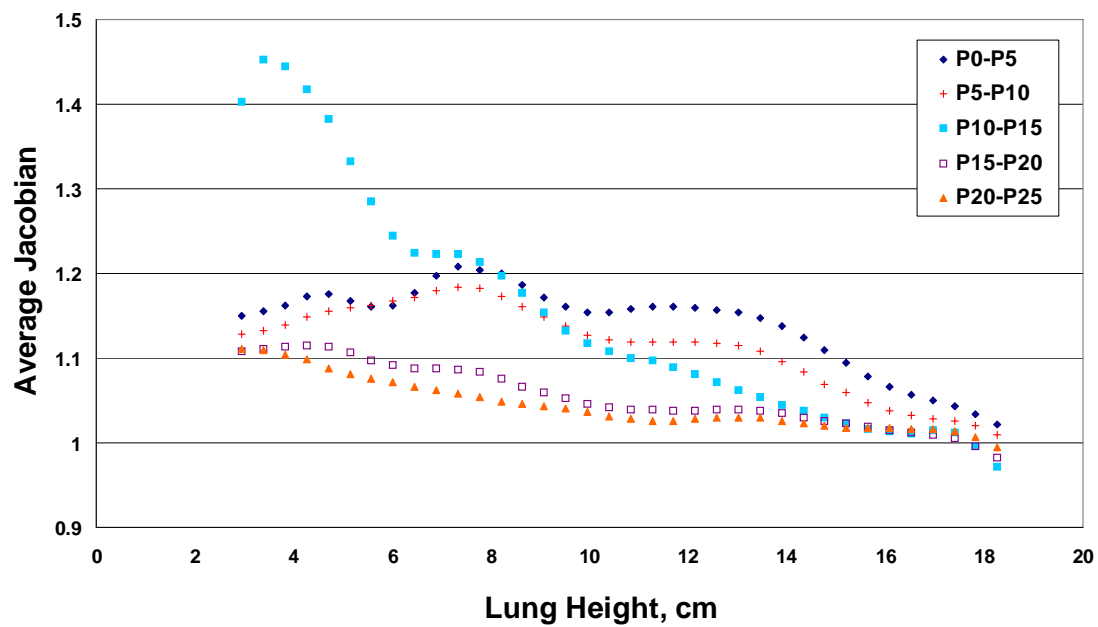
(b)
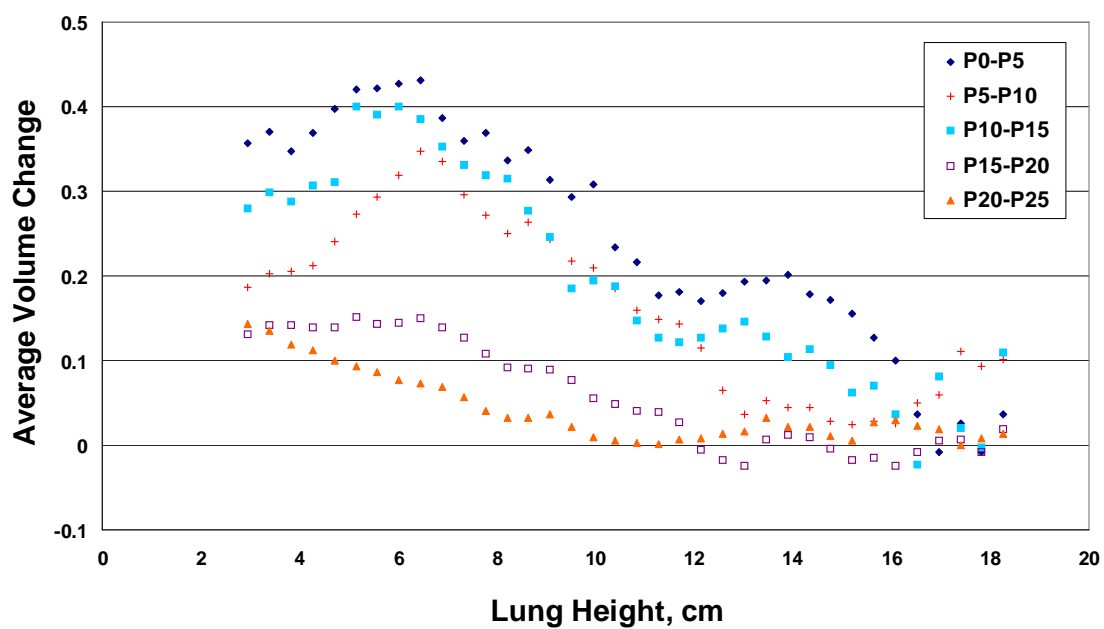

(c)

Figure C.2 continued.

C.3 Sheep AS70078

(a)

Figure C.3: The sV, Jacobian and intensity-based regional volume change measurements vs. lung height for sheep AS70078. (a) Average $\pm$ standard deviation of sV analyzed from Xe-CT at $P0$ vs. lung height; (b) average Jacobian for all 5 cm pressure change pairs vs. lung height; and (c) intensity-based regional volume change for all 5 cm pressure change pairs vs. lung height.
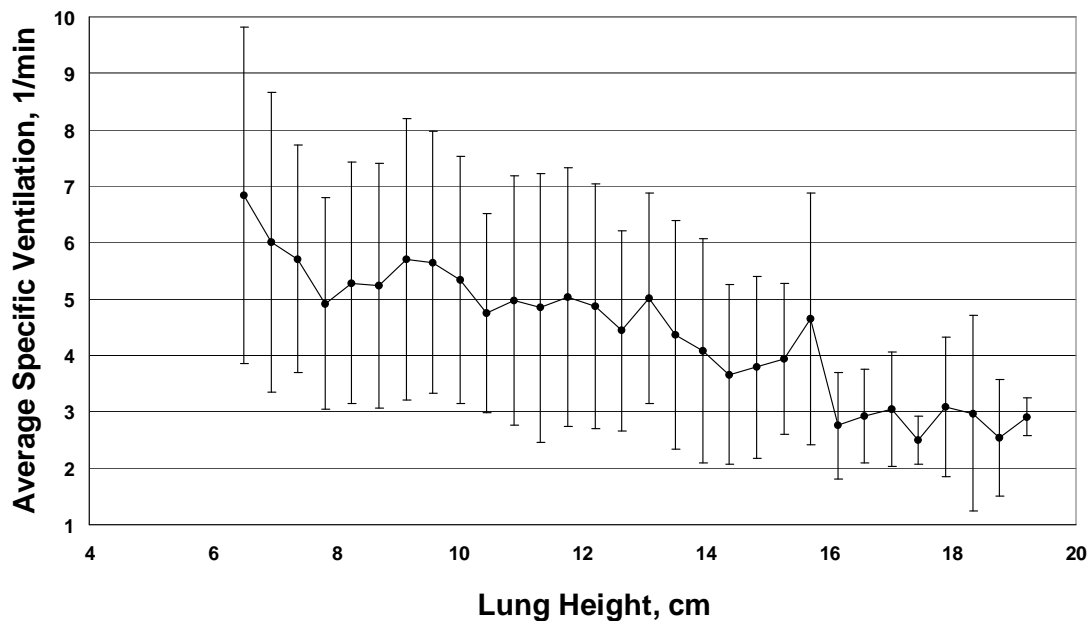
(b)

(c)

Figure C.3 continued.

C.4   Sheep AS70079

(a)

Figure C.4: The sV, Jacobian and intensity-based regional volume change measurements vs. lung height for sheep AS70079. (a) Average $\pm$ standard deviation of sV analyzed from Xe-CT at $P0$ vs. lung height; (b) average Jacobian for all 5 cm pressure change pairs vs. lung height; and (c) intensity-based regional volume change for all 5 cm pressure change pairs vs. lung height.
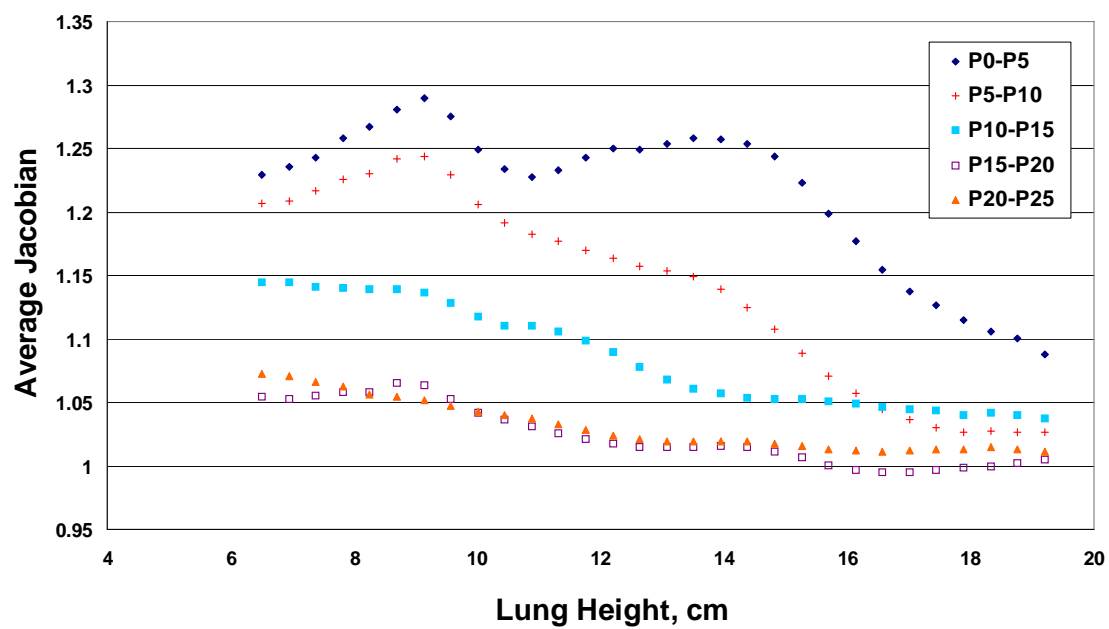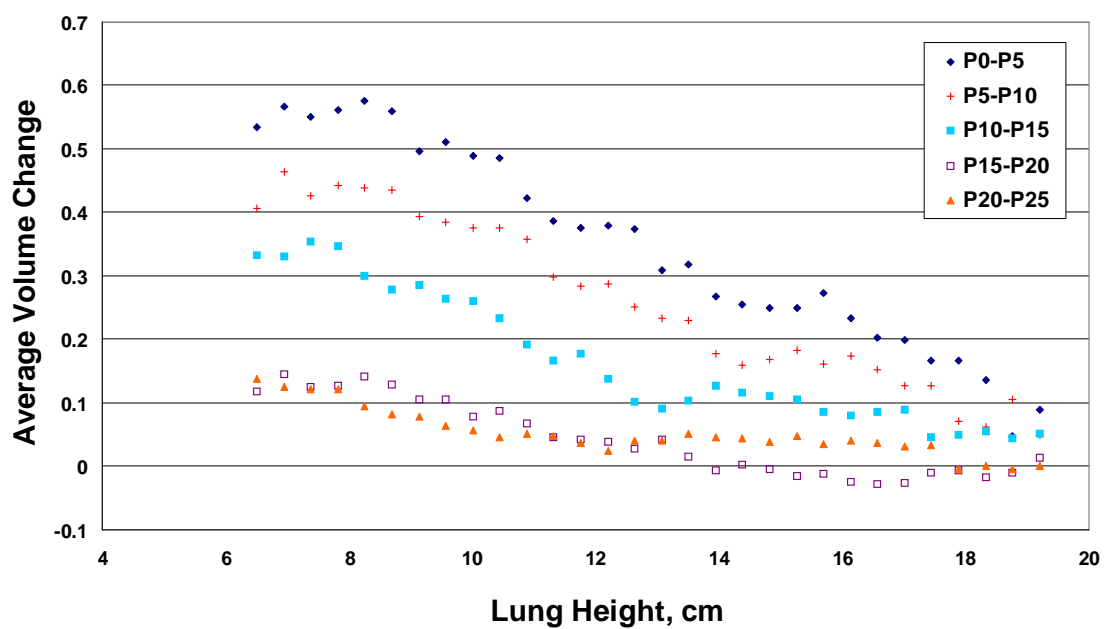
(b)

(c)

Figure C.4 continued.

C.5 Sheep AS70080

(a)

Figure C.5: The sV, Jacobian and intensity-based regional volume change measurements vs. lung height for sheep AS70080. (a) Average ± standard deviation of sV analyzed from Xe-CT at $P0$ vs. lung height; (b) average Jacobian for all 5 cm pressure change pairs vs. lung height; and (c) intensity-based regional volume change for all 5 cm pressure change pairs vs. lung height.
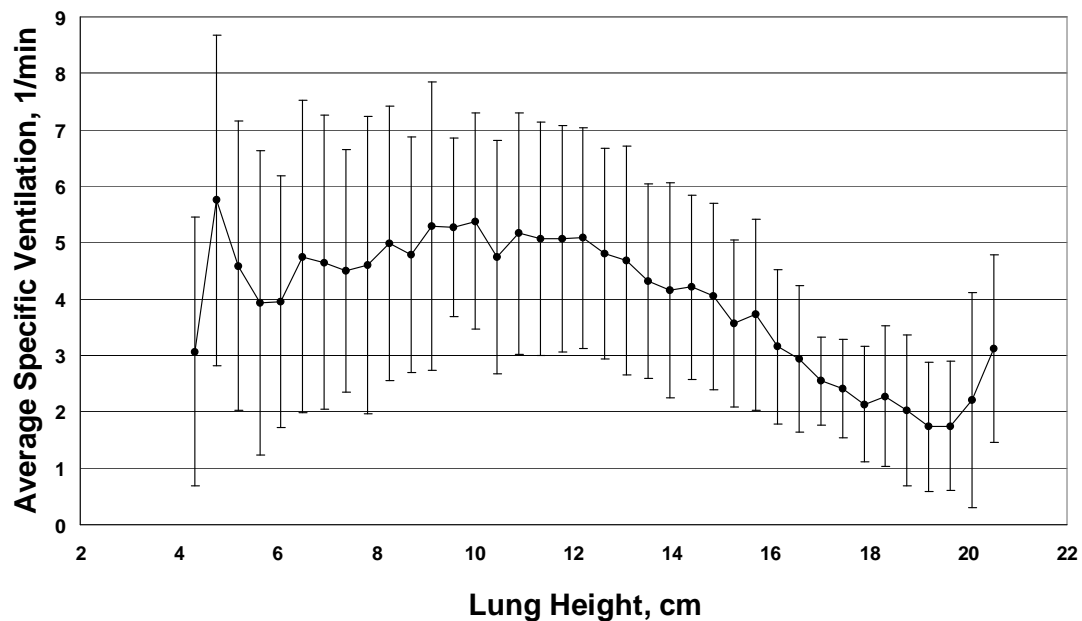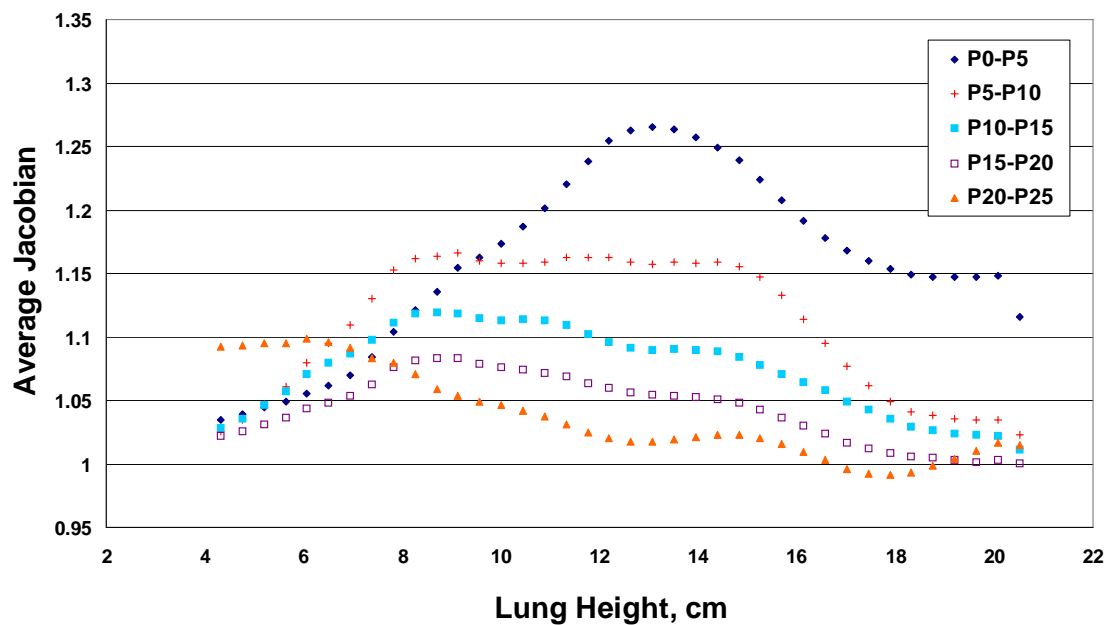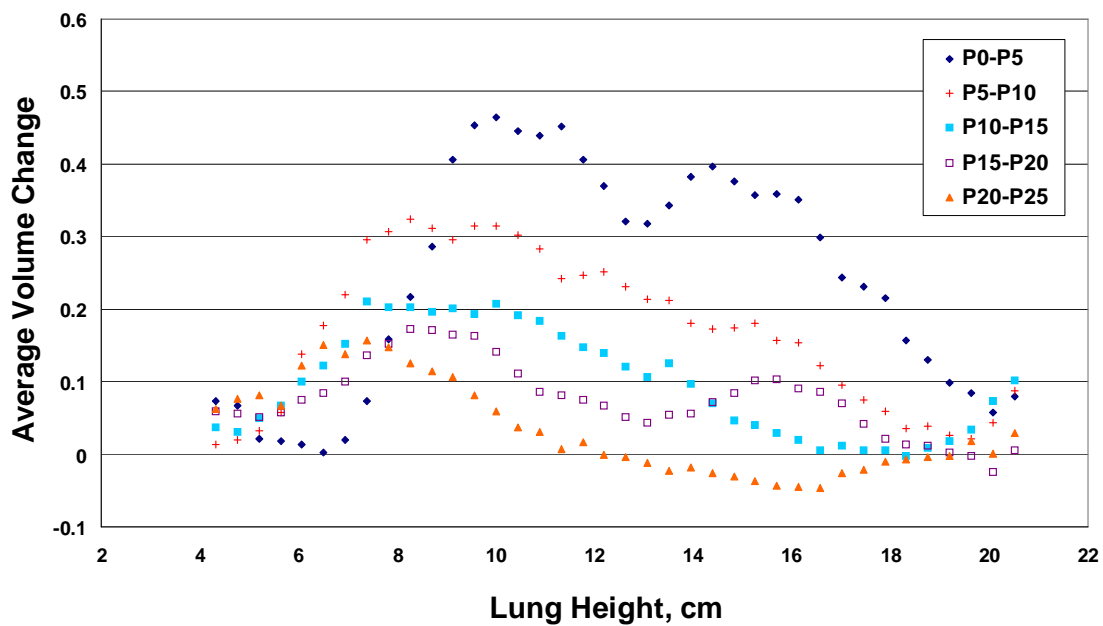
(b)

(c)

Figure C.5 continued.

REFERENCES

[1] Y. Amit. A non-linear variational problem for image matching. *SIAM Journal on Scientific Computation*, 15(1):207–224, January 1994.

[2] Deokiee Chon, Brett A. Simon, Kenneth C. Beck, Hidenori Shikata, Osama I. Saba, Chulho Won, and Eric A. Hoffman. Differences in regional wash-in and wash-out time constants for xenon-CT ventilation studies. *Respiratory Physiology & Neurobiology*, 148:65–83, 2005.

[3] Gary E. Christensen, Xiujuan Geng, Jon G. Kuhl, Joel Bruss, Thomas J. Grabowski, John S. Allen, Imran A. Pirwani, Michael W. Vannier, and Hanna Damasio. Introduction to the non-rigid image registration evaluation project (nirep). In *3rd International Workshop on Biomedical Image Registration*, LCNS 4057, pages 128–135. Springer-Verlag, July 2006.

[4] Gary E. Christensen, J. H. Song, W. Lu, I. El Naqa, and D. A. Low. Tracking lung tissue motion and expansion/compression with inverse consistent image registration and spirometry. *Med Physics*, 34(6):2155–2165, June 2007.

[5] G.E. Christensen. Consistent linear-elastic transformations for image matching. In A. Kuba and M. Samal, editors, *Information Processing in Medical Imaging*, LCNS 1613, pages 224–237, Berlin, June 1999. Springer-Verlag.

[6] G.E. Christensen and H.J. Johnson. Consistent image registration. *IEEE Trans. Med. Imaging*, 20(7):568–582, July 2001.

[7] G.E. Christensen and H.J. Johnson. Invertibility and transitivity analysis for nonrigid image registration. *Journal of Electronic Imaging*, 12(1):106–117, Jan. 2003.

[8] G.E. Christensen, S.C. Joshi, and M.I. Miller. Volumetric transformation of brain anatomy. *IEEE Trans. on Med. Imaging*, 16(6):864–877, December 1997.

[9] G.E. Christensen, R.D. Rabbitt, and M.I. Miller. 3D brain mapping using a deformable neuroanatomy. *Physics in Medicine and Biology*, 39:609–618, 1994.

[10] G.E. Christensen, J.H. Song, I.E. Naqa, W. Lu, and D.A. Low. Tracking lung motion: Correlating inverse consistent image registration and spirometry. In *Proceedings of the 14th International Conference on the Use of Computers in Radiation Therapy*, pages 493–496, Seoul, Korea, May 9-14, 2004.

[11] A. Collignon, F. Maes, D. Delaere, D. Vandermeulen, P. Suetens, and G. Marchal. Automated multi-modality image registration based on information theory. In Y. Bizais, C. Braillot, and R. Di Paola, editors, *Information Processing in Medical Imaging*, volume 3, pages 263–274. Kluwer Academic Publishers, Boston, June 1995.

[12] Thomas Guerrero, Kevin Sanders, Edward Castillo, Yin Zhang, L. Bidaut, and T. Pan R. Komaki. Dynamic ventilation imaging from four-dimensional computed tomography. *Phys Med Biol.*, 51(4):777–791, Feb. 21 2006.

[13] Thomas Guerrero, Kevin Sanders, Josue Noyola-Martinez, Edward Castillo, Yin Zhang, Richard Tapia, Rudy Guerra, Yerko Borghero, and Ritsuko Komaki. Quantification of regional ventilation from treatment planning CT. *Int. J. Radiation Oncology Biol. Phys.*, 62(3):630–634, Jul 1 2005.

[14] W.M. Wells III, P. Viola, H. Atsumi, S. Nakajima, and R. Kikinis. Multi-modal volume registration by maximization of mutual information. *Medical Image Analysis*, 1(1):35–51, 1996.

[15] Hans J. Johnson. Method for consistent linear-elastic medical image registration. Master's thesis, Department of Electrical and Computer Engineering, The University of Iowa, Iowa City, IA 52242, May 2000.

[16] H.J. Johnson and G.E. Christensen. Consistent landmark and intensity-based image registration. *IEEE Trans. Med. Imaging*, 21(5):450–461, 2002.

[17] F. Maes, A. Collignon, D. Vandermeulen, G. Marchal, and P. Suetens. Multimodality image registration by maximization of mutual information. *IEEE Transactions on Medical Imaging*, 16(2):187–198, April 1997.

[18] C Marcucci, D Nyhan, and B A Simon. Distribution of pulmonary ventilation using Xe-enhanced computed tomography in prone and supine dogs. *JAP*, 90(2):421–430, 2001.

[19] D. Mattes, D.R. Haynor, H. Vesselle, T.K. Lewellen, and W. Eubank. Pet-ct image registration in the chest using free-form deformations. *IEEE Transactions on Medical Imaging*, 22(1):120–128, Jan. 2003.

[20] Joseph M. Reinhardt, Kai Ding, Kunlin Cao, Gary E. Christensen, Eric A. Hoffman, and Shalmali V. Bodas. Registration-based estimates of local lung tissue expansion compared to xenon-ct measures of specific ventilation. *Medical Image Analysis*, In press.

[21] B A Simon and C Marcucci. Parameter estimation and confidence intervals for Xe-CT ventilation studies: A Monte Carlo approach. *JAP*, 84(2):709–716, 1998.

[22] BA Simon. Non-invasive imaging of regional lung function using X-ray computed tomography. *J Clin Monit Comput*, 16(5-6):433–442, 2000.

[23] Tessa A. Sundaram and James C. Gee. Towards a model of lung biomechanics: pulmonary kinematics via registration of serial lung images. *Medical Image Analysis*, 9(6):524–537, 2005.

[24] Tessa A. Sundaram and James C. Gee. Quantitative comparison of registration-based lung motion estimates from whole-lung mr images and corresponding two-dimensional slices. In *Proc. ISMRM 15th Mtg*, page p.3039, 2007.

[25] J. K. Tajik, D. Chon, C.-H. Won, B. Q. Tran, and E. A. Hoffman. Subsecond multisection CT of regional pulmonary ventilation. *AR*, 9:130–146, 2002.

[26] P. Viola and W. M. Wells III. Alignment by maximization of mutual information. *International Journal of Computer Vision*, 24(2):137–154, 1997.